Subduction-related Volatile Recycling and Magma Generation beneath Central Mexico: Insights from Melt Inclusions, Oxygen Isotopes and Geodynamic Models

EMILY R. JOHNSON[1,2]*, PAUL J. WALLACE[1], HUGO DELGADO GRANADOS[3], VLAD C. MANEA[4], ADAM J. R. KENT[1], ILYA N. BINDEMAN[1] AND COLLEEN S. DONEGAN[1]†

[1]DEPARTMENT OF GEOLOGICAL SCIENCES, UNIVERSITY OF OREGON, EUGENE, OR 97403, USA

[2]CODES ARC CENTRE OF EXCELLENCE IN ORE DEPOSITS, UNIVERSITY OF TASMANIA, PRIVATE BAG 126, HOBART, TASMANIA 7001, AUSTRALIA

[3]INSTITUTO DE GEOFÍSICA, UNIVERSIDAD NACIONAL AUTÓNOMA DE MÉXICO, DISTRITO FEDERAL, 04510 MEXICO

[4]COMPUTATIONAL GEODYNAMICS LABORATORY, CENTRO DE GEOCIENCIAS, UNIVERSIDAD NACIONAL AUTÓNOMA DE MÉXICO, JURIQUILLA, QUERÉTARO, 76230, MEXICO

The subduction-related Michoacán–Guanajuato Volcanic Field (MGVF) in central Mexico contains ~900 cinder cones and numerous larger shield volcanoes of Late Pliocene to Holocene age. We present data for major, trace and volatile (H_2O, CO_2, S, Cl) elements in olivine-hosted melt inclusions from eight calc-alkaline cinder cones with primitive magma characteristics and one more evolved alkali basalt tuff ring. The samples span a region extending from the volcanic front to ~175 km behind the front. Relationships between H_2O and incompatible trace elements are used to estimate magmatic H_2O contents for 269 additional volcanic centers across the MGVF and central Mexico. The results show that magmatic H_2O remains high (3–5·75 wt %) for large distances (~150 km) behind the front. Chlorine and S concentrations are strongly correlated with melt H_2O and are also high across most of the arc (700–1350 ppm Cl, 1500–2000 ppm S). The alkali basalt, located far behind the front (~175 km), has much lower volatile contents (<1·5 wt % H_2O, 200 ppm Cl, 500 ppm S), and is compositionally similar to other melts erupted in this region. Oxygen isotope ratios of olivine phenocrysts (5·6–6‰) from the calc-alkaline samples are higher than for typical mantle-derived magmas but do not vary systematically across the arc. Calc-alkaline samples have high large ion lithophile element concentrations relative to Nb and Ta, as is typical of subduction-related magmas, but alkali basalt samples far behind the front have high Nb and Ta and lack enrichments in fluid-mobile elements. Modeling based on volatiles and trace elements suggests that the calc-alkaline magmas were generated by 6–15% partial melting of a variably depleted mantle wedge that was fluxed with H_2O-rich components from the subducted slab. In contrast, the alkali basalts formed by small degrees of decompression melting of an ocean island basalt source that had not been fluxed by slab-derived components. Based on high $\delta^{18}O_{olivine}$ values and trace element characteristics, the H_2O-rich subduction components added to the mantle wedge beneath the MGVF are likely to be mixtures of oceanic crust derived fluids and sediment melts. Integrating these results with new 2-D thermo-mechanical models of the subduction zone beneath the MGVF, we demonstrate that the present-day plate configuration beneath the MGVF causes fluids to be released beneath the forearc and volcanic front, and that sediment melts can be produced beneath the volcanic front by the waning stages of fluid released from the oceanic crust percolating through already dehydrated sediments. Down-dragging of serpentine- and chlorite-bearing peridotite in the lowermost mantle wedge probably plays a

*Corresponding author. Telephone: +61 3 6226 7210. Fax: +61 3 6226 7662. E-mail: Emily.Johnson@utas.edu.au
†Present address: Department of Geology, Northern Arizona University, Flagstaff, AZ 86011, USA.

role in fluid transport from the forearc to beneath the arc. H_2O-rich magmas located more than ~50 km behind the volcanic front can be explained by mantle hydration related to a shallower slab geometry that existed at ~3 Ma. Rollback of the slab over the last ~2 Myr has resulted in strong mantle advection that forms low-H_2O, high-Nb alkali basaltic magmas by decompression melting far behind the present-day volcanic front.

KEY WORDS: *subduction; partial melting; oxygen isotopes; volatiles; devolatilization; melt inclusions*

INTRODUCTION

Water plays an important role in arc magmatism because fluids and/or hydrous melts released from the subducted slab rise into the mantle wedge, lowering its melting temperature and thus triggering magma formation (McBirney, 1969; Fyfe & McBirney, 1975; Anderson, 1982; McCulloch & Gamble, 1991; Luhr, 1992; Gaetani *et al.*, 1993; Sisson & Grove, 1993; Stolper & Newman, 1994; Gaetani & Grove, 1998). Although some arc magmas appear to be produced by decompression melting and have low volatile contents (Sisson & Layne, 1993; Sisson & Bronto; 1998; Grove *et al.*, 2002; Cervantes & Wallace, 2003), most arc magmas result from such flux melting of the mantle wedge. Magmas in volcanic arcs often erupt explosively and have been shown to contain high concentrations of volatiles (H_2O, CO_2, S, Cl), with H_2O contents of 3–5 wt % commonly measured in arc basalts worldwide (Wallace, 2005; Wade *et al.*, 2006; Benjamin *et al.*, 2007; Johnson *et al.*, 2008; Auer *et al.*, 2009; Roberge *et al.*, 2009).

Whereas there have been numerous studies of the volatile contents of individual arc volcanoes in recent years (e.g. Gurenko *et al.*, 2005; Wade *et al.*, 2006; Benjamin *et al.*, 2007), there have been fewer studies of volatile variations across arcs (Walker *et al.*, 2003; Portnyagin *et al.*, 2007; Sadofsky *et al.*, 2008). Because volatiles are added to the mantle wedge by an H_2O-rich subduction-derived component, variations in volatile concentrations across a volcanic arc reflect dehydration in the subducting plate and melting processes in the mantle wedge. For example, low concentrations of H_2O and fluid-mobile elements (e.g. B, Ba) measured in some arc magmas behind the volcanic front have suggested that the flux of H_2O-rich components decreases behind the volcanic front (Hochstaeder *et al.*, 1996; Walker *et al.*, 2003). Furthermore, across-arc datasets that include volatiles, trace elements, and stable and/or radiogenic isotopes are useful for determining the composition and origin of the subduction-derived components added to the mantle wedge (Stolper & Newman, 1994; Grove *et al.*, 2002; Eiler *et al.*, 2005; Wysoczanski *et al.*, 2006; Portnyagin *et al.*, 2007; Sadofsky *et al.*, 2008).

In this study, we present the results of an across-arc investigation of the volatile and major and trace element composition of olivine-hosted melt inclusions from the Michoacán–Guanajuato Volcanic Field (MGVF) of central Mexico. The primitive nature of the MGVF magmas (e.g. Fo_{87-90} olivine in many samples) makes it possible to calculate both primary melt compositions and mantle volatile contents. These data, combined with oxygen isotope ratios of olivine phenocrysts and new 2-D thermal models of the subduction zone beneath the MGVF, allow us to estimate the source and composition of H_2O-rich subduction components added to the mantle wedge and to constrain slab dehydration depths, temperatures in the mantle wedge and the effect of fluid fluxing on mantle melting.

GEOLOGICAL SETTING— MICHOACÁN–GUANAJUATO VOLCANIC FIELD, MEXICO

Volcanism in Mexico is related to subduction of the Rivera (to the NW) and Cocos plates beneath the North American plate at the Middle America Trench (MAT, Fig. 1). The Cocos plate subducting beneath the MGVF is relatively young (11–17 Ma at the trench; Pardo & Suárez, 1995), and thus the Trans-Mexican Volcanic Belt (TMVB) is a 'warm-slab' subduction zone (Kirby *et al.*, 2002). The TMVB is a broad zone of volcanism that spans the country from west to east and contains several discrete volcanic fields. The MGVF is located to the west of Mexico City and contains ~900 cinder cones and numerous larger shield volcanoes (Hasenaka & Carmichael, 1985), making it an ideal locality for this type of study. First, it has an abundance of young (Holocene) cinder cones (Hasenaka & Carmichael, 1985) that are distributed over large distances behind the volcanic front. Second, most of the cinder cones are basaltic to basaltic andesite in composition, and published bulk-rock geochemical data for many cones (e.g. Hasenaka & Carmichael, 1985) allowed us to sample those that are compositionally most primitive.

SAMPLES AND METHODS
Melt inclusions and olivine hosts

Tephra was sampled from nine monogenetic volcanoes (eight cinder cones and one maar) across the MGVF at varying distances from the Middle America Trench ranging from the volcanic front to roughly 175 km behind the front (Fig. 2). When possible, samples were taken from the basal layers of the tephra blanket (in contact with the soil) to compare the earliest erupted material at each volcano, which commonly has the most primitive compositions of the sequence (e.g. Johnson *et al.*, 2008). Major and trace element compositions of bulk tephra samples analyzed by X-ray fluorescence (XRF) and inductively coupled plasma-mass spectrometry (ICP-MS) in the GeoAnalytical Laboratory at Washington State
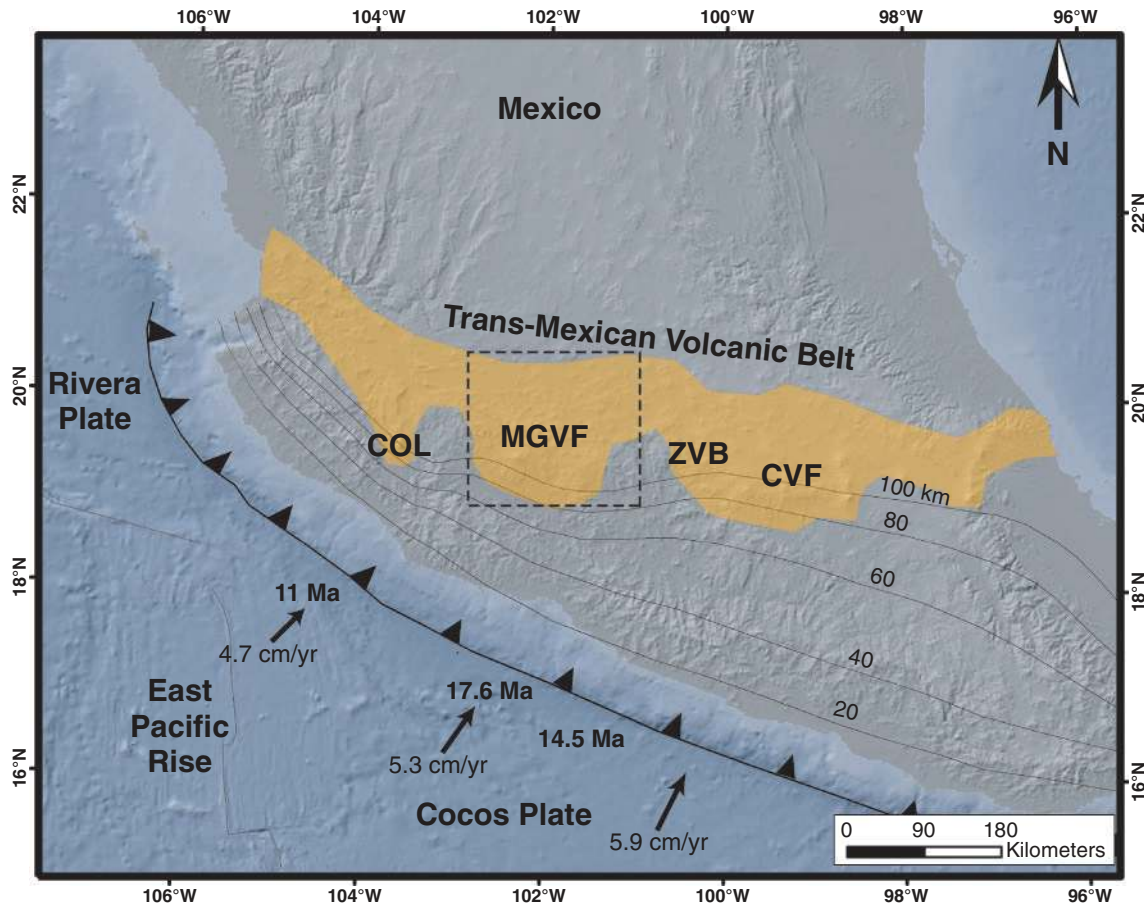
Fig. 1. The Trans-Mexican Volcanic Belt and offshore plate boundaries. Ages of the subducting Cocos plate near the Middle America Trench and contours to the top of the subducting slab are from Pardo & Suárez (1995). Arrows show convergence rates between the Cocos and North American plates (DeMets *et al.*, 1994). MGVF, Michoacán–Guanajuato Volcanic Field; ZVB, Zitácuaro–Valle de Bravo volcanic field; CVF, Chichináutzin Volcanic Field; COL, Colima Volcano.

University are reported in Electronic Appendix 1 (all Electronic Appendices can be downloaded from the *Journal of Petrology* website at http://www.petrology .oxfordjournals.org).

Loose olivine crystals from the tephra samples were separated and washed, and those with suitable melt inclusions (fully enclosed, glassy) were prepared for analysis. Major and minor element (including S and Cl) analyses of melt inclusions and their olivine hosts were obtained using a Cameca SX-100 electron microprobe at the University of Oregon using a 15 kV accelerating voltage, 10 nA beam current (20 nA for olivine analyses), and a beam diameter of 10 μm. The beam current was increased to 40 nA when analyzing S and Cl, and on-peak counting times were increased to 80 s for S and 100 s for Cl. Based on previous analyses of FeO and Fe_2O_3 in MGVF lavas (Hasenaka & Carmichael, 1985), the oxidation states of basaltic magmas in the MGVF were estimated to be NNO + 0·5 to NNO +1 [where NNO is the nickel–nickel oxide buffer; using the method of Kress & Carmichael

(1991)], which corresponds to a SKα peak position that is intermediate between those for anhydrite and pyrite (∼30% of the full shift between pyrite and anhydrite; Wallace & Carmichael, 1994). For the S analyses, we used an anhydrite standard measured using the sulfate SKα peak position, whereas the unknowns were analyzed using a SKα peak position between pyrite and anhydrite. To minimize loss of counts caused by alkali migration (Na, K) and corresponding increases in Si and Al we used a volatile correction program that fits an exponential function to the count rates for these elements and then extrapolates back to time zero. A combination of glass and mineral standards was used in the microprobe analyses. Trace element concentrations of at least three melt inclusions from each cinder cone were measured using laser ablation (LA)- ICP-MS in the W. M. Keck Collaboratory for Plasma Mass Spectrometry at Oregon State University using a DUV 193 nm ArF Excimer laser and a VG ExCell quadrupole ICP-MS system. Details of the technique have been summarized by Kent *et al.* (2004).
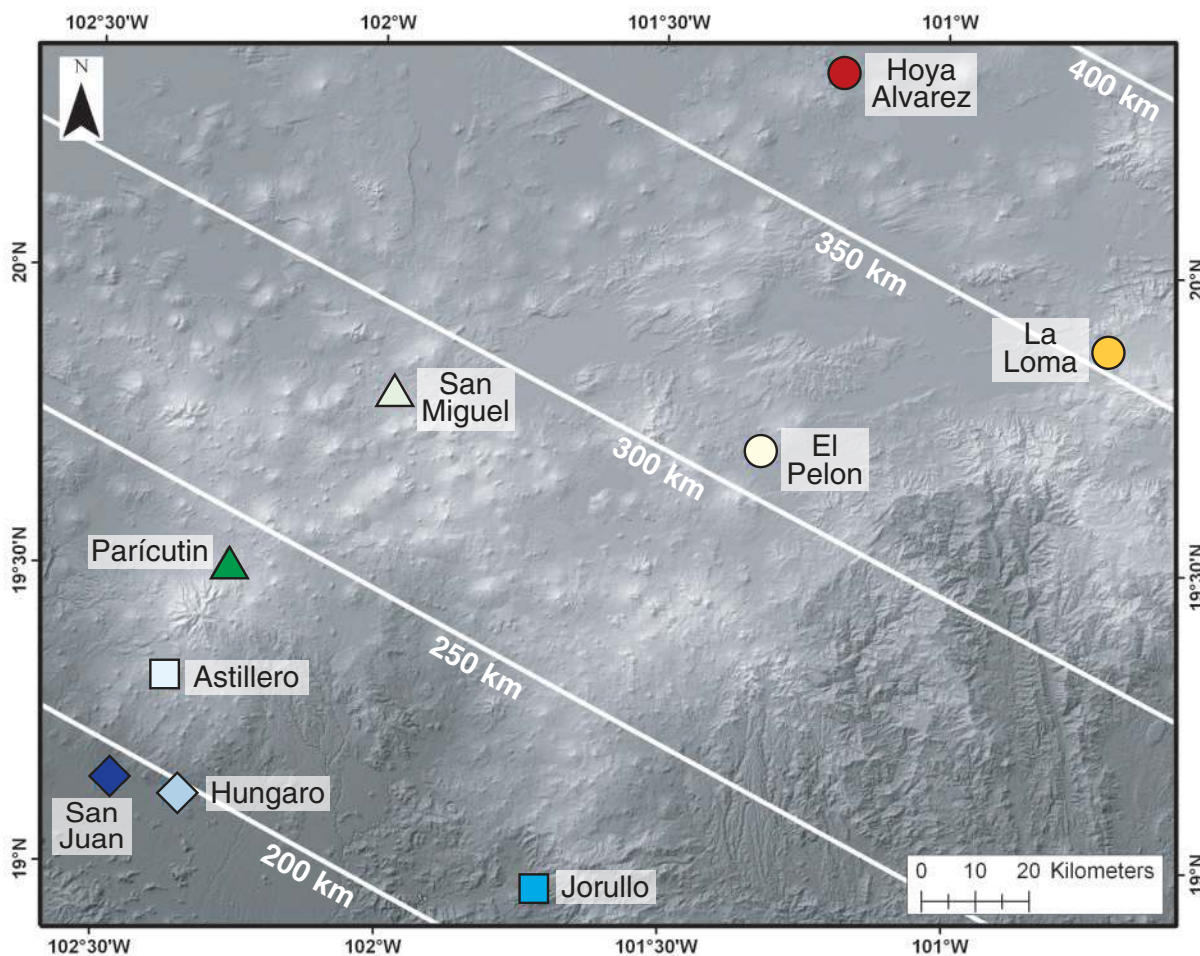
Fig. 2. Sample locations from this study within the MGVF. White lines show distance from the Middle America Trench (MAT). Volcanic front is located ~200 km from the MAT.

Water and CO_2 concentrations in melt inclusions were analyzed by Fourier transform infrared spectroscopy (FTIR) at the University of Oregon. Concentrations of H_2O and CO_2 were calculated using Beer's law: $c = MA/\rho d\varepsilon$, where M is the molecular weight of H_2O or CO_2, A is the measured absorbance of the band of interest, ρ is the density of basaltic glass [calculated following Luhr (2001)], d is the thickness of the melt inclusion and ε is the molar absorption coefficient. In most samples, water concentrations were calculated using the total OH peak at $3550\,cm^{-1}$ and an absorption coefficient of 63 ± 3 L/mol cm (P. Dobson et al., unpublished data, cited by Dixon et al., 1995). In some instances, however, total H_2O was calculated by summing the average concentrations of the molecular H_2O peaks at $1630\,cm^{-1}$ and $5200\,cm^{-1}$ together with the concentration from the OH^- peak at $4500\,cm^{-1}$. In these cases absorption coefficients were calculated based on major element compositions (Dixon et al., 1995). CO_2 was measured using the carbonate peaks at 1515 and

$1435\,cm^{-1}$; an absorption coefficient was calculated (typically 290–300 L/mol cm) based on the major element composition of each sample (Dixon & Pan, 1995). The background around the carbonate peaks is complex, and thus it is necessary to subtract a carbonate-free, basaltic reference glass spectrum from each sample spectrum to obtain a flat background (Dixon et al., 1995). We measured the absorbance of the carbonate doublet peaks using a peak-fitting program (unpublished program by S. Newman). Based on uncertainties in thickness measurements and absorbance values, average 1 standard deviation (S.D.) uncertainty for H_2O is ± 0.2 wt % and for CO_2 ± 80 ppm.

All melt inclusion data were corrected for post-entrapment crystallization of olivine (Sobolev & Chaussidon, 1996) and diffusive loss of Fe (Danyushevsky et al., 2000). The data were corrected for post-entrapment crystallization by adding equilibrium olivine, in incremental fractions of 0.1 wt %, back into each melt inclusion

until the melt inclusion composition was in equilibrium with its host olivine (as analyzed by electron microprobe). There are two variables used in calculating the equilibrium olivine composition: the K_D value and the FeO/FeO^T ratio. We used a K_D of 0.3 ± 0.01 (Toplis, 2005) and FeO/FeO^T values (0.7–0.8) based on whole-rock lava data (Hasenaka & Carmichael, 1985; Righter & Carmichael, 1993; Luhr, 2001). Following the procedure of Danyushevsky *et al.* (2000) we also corrected the inclusions, if necessary, for post-entrapment Fe loss. We plotted the melt inclusion FeO^T vs MgO and the bulk tephra XRF data and/or whole-rock data for each cone. Inclusions with low FeO^T compared with the whole-rock trends had FeO added back into their compositions until they matched the whole-rock trend. For some cones, there were not sufficient data to define a whole-rock trend. Samples from these cones contained olivine phenocrysts only, so we assumed that at the time of trapping, melts had FeO^T contents that fell along an olivine fractionation line emanating from the whole-rock composition. All major, minor, and volatile element data corrected for post-entrapment crystallization and Fe loss are reported in Table 1, and analyzed (uncorrected) values for all inclusions are reported in Electronic Appendix 2. Corrected trace element analyses are shown in Table 2, and uncorrected values are given in Electronic Appendix 3.

Oxygen isotopes

Oxygen isotopes were measured on separated olivine crystals that did not contain obvious melt inclusions and that had minimal inclusions of spinel or other oxides. The olivines were cleaned in HBF_4 to remove adhering glass. Isotope analyses were performed at the University of Oregon using the CO_2 laser fluorination technique (as described by Bindeman *et al.*, 2005; Bindeman, 2008; Martin *et al.*, 2009) and BrF_5 as reagent on multiple grains of olivine. Oxygen was converted to CO_2 gas in a platinum–graphite converter, and the gas was measured and then analyzed on an MAT 253 mass spectrometer. Unknowns were corrected based on the values of standards run in the same analytical session: 5.75‰ Gore Mt. Garnet (Valley *et al.*, 1995) and 5.35‰ San Carlos Olivine (Eiler, 2001), with 1 S.D. on standards in each of three analytical sessions ranging from 0.02 to 0.08‰. The results on the unknowns run in different analytical sessions were corrected to the quoted standard values on the VSMOW scale to account for day-to-day variability, and the correction ranged from +0.32 to +0.20‰. Measurements were made on two to three samples of 1.1−2.0 mg of olivine separated from the tephra from each cone. Precision on replicate and triplicate analyses was ± 0.08−0.16‰ (1σ), slightly poorer than the reproducibility of the standards. This suggests possible small-scale heterogeneity of olivine populations and/or that the presence of spinel inclusions in the olivines affected the precision of some analyses. Oxygen isotope data are reported in Table 3.

Geodynamic modeling of the subducted slab and mantle wedge beneath the MGVF

Modeling of subduction beneath the MGVF was performed by using a system of 2-D Stokes' equations and a 2-D steady-state heat transfer equation, assuming strong temperature-dependent viscosity in the mantle wedge [see details given by Manea *et al.* (2004, 2005)]. The rheological parameters used in the thermal models are as follows: a reference mantle wedge viscosity (η_o) of 10^{20} Pa s and an activation energy for olivine (E_a) of 250 kJ/mol. Variations in E_a from 150 to 300 kJ/mol result in only very small temperature increases in the mantle wedge (<25°C; Manea *et al.*, 2005). A small degree of frictional heating was introduced ($\mu = 0.017$) along the thrust fault between the subducting and continental plates. Justification and validation of the model parameters have been discussed by Manea *et al.* (2004, 2005). Models were created for the present-day slab geometry and a flat-slab geometry at 3 Ma, which is assumed to be similar to the present-day geometry to the SE of the MGVF (i.e. slab depth of 100 km at 350 km from the trench, Fig. 1). In both models, the convergence rate is 5 cm/year and the slab age at the MAT is 13 Ma.

RESULTS
Olivine and melt inclusion compositions

The cinder cones sampled in this study erupted medium-K calc-alkaline basalt to basaltic andesite, whereas the tuff ring, Hoya Alvarez, located farthest behind the volcanic front, erupted alkali basalt. The calc-alkaline tephra and lava have mostly $Fo_{82–91}$ olivine and Mg-numbers of 59–78 (this study; Hasenaka & Carmichael, 1985), and Hoya Alvarez tephra and lava have $Fo_{63–79}$ olivine and an Mg-number of 56. Olivine-hosted melt inclusions from the calc-alkaline centers mostly contain 50–56 wt % SiO_2 and 4–10 wt % MgO, whereas those from Hoya Alvarez contain 46–49% SiO_2 and 3–6 wt % MgO (all values have been corrected for post-entrapment crystallization and Fe loss). Major and trace element compositions of the melt inclusions are generally similar to the compositions of the bulk tephra and lava from their respective cones. The exceptions are San Miguel and La Loma, both of which contain melt inclusions that define two populations based on olivine compositions and trace element ratios. From these centers, the least evolved melt inclusion compositions (those in Fo-rich olivine) were used for the primary melt composition calculations (discussed below).

Volatile concentrations

Melt inclusions at each volcano contain highly variable H_2O and CO_2 concentrations (Table 1). For the calc-alkaline cones, values are ≤5.75 wt % H_2O and ≤1200 ppm

Table 1: Major elements and volatiles in melt inclusions (corrected values)

Cerro San Juan

	CSJ-1	CSJ-5	CSJ-31	CSJ-32	CSJ-33	CSJ-37	CSJ-39	CSJ-41	CSJ-44	CSJ-45s	CSJ-45L	CSJ-46	CSJ-48	CSJ-51
SiO_2	51·79	51·52	50·40	52·01	51·29	—	50·61	51·59	51·54	52·30	51·79	51·43	50·91	51·56
TiO_2	1·18	1·04	1·03	1·08	1·07	—	1·23	1·31	0·97	1·08	1·11	0·93	1·17	1·19
Al_2O_3	17·64	18·11	18·54	17·21	17·92	—	18·74	18·79	18·35	18·04	18·12	18·36	18·59	17·95
FeO^T	9·35	9·24	9·41	9·48	9·41	—	9·41	9·03	9·15	9·25	9·29	9·41	9·26	8·97
MnO	0·08	0·12	0·09	0·14	0·10	—	0·10	0·11	0·11	0·06	0·08	0·10	0·06	0·11
MgO	7·12	6·76	7·31	7·17	7·09	—	6·88	6·26	6·62	6·93	6·95	6·49	7·16	6·83
CaO	8·34	8·58	8·68	7·88	8·76	—	8·35	8·24	8·37	7·36	8·04	8·53	8·21	8·43
Na_2O	3·39	3·52	3·48	3·72	3·28	—	3·52	3·52	3·71	3·65	3·19	3·52	3·45	3·79
K_2O	0·86	0·84	0·86	1·07	0·85	—	0·93	0·93	0·92	1·11	1·14	0·98	0·95	0·90
P_2O_5	0·23	0·27	0·21	0·23	0·23	—	0·25	0·22	0·25	0·23	0·29	0·24	0·23	0·25
H_2O	2·9	2·1	1·7	0·8	2·6	3·0	2·4	2·8	1·5	2·8	1·5	1·9	1·7	1·5
CO_2 ppm	660	b.d.	b.d.	b.d.	1170	1800	b.d.	970	b.d.	b.d.	b.d.	530	b.d.	590
S ppm	830	990	960	450	850	—	1050	1100	1080	1230	1160	1040	1100	1020
Cl ppm	580	600	620	570	480	—	830	790	820	830	780	780	770	740
Olivine (Fo%)	84·6	84·2	84·6	84·5	84·5	—	84·1	83·6	84·1	84·5	84·5	83·3	84·9	84·8
% ol added*	6·3	4·5	11·6	7·3	6·5		6	1·7	4·7	5	4·9	5·2	6·1	4

Cerro el Hungaro

	CeH 15	CeH 24	CeH 39a	CeH 39b	CeH 86	CeH 88	CeH 91	CeH 93	CeH 95	CeH 98	CeH 99
SiO_2	53·53	54·21	55·80	54·53	52·93	53·98	53·64	52·95	53·33	52·56	53·12
TiO_2	0·95	0·97	0·93	0·81	0·91	0·85	0·93	1·00	0·92	0·96	0·92
Al_2O_3	18·56	18·09	16·05	17·43	17·65	17·47	18·20	18·42	18·71	19·41	18·15
FeO^T	7·52	7·38	7·54	7·20	7·59	7·35	7·39	7·82	7·40	7·47	7·71
MnO	0·07	0·10	0·10	0·08	0·08	0·08	0·10	0·08	0·10	0·06	0·09
MgO	5·92	7·31	7·39	7·00	7·83	7·71	6·86	7·29	6·81	7·01	7·17
CaO	8·27	8·22	6·68	7·48	7·87	7·60	7·77	8·04	8·38	8·07	7·95
Na_2O	4·09	2·61	4·07	4·23	4·13	3·90	3·98	3·51	3·55	3·54	4·06
K_2O	0·85	0·87	1·22	1·01	0·80	0·84	0·94	0·70	0·64	0·73	0·65
P_2O_5	0·24	0·24	0·22	0·23	0·21	0·21	0·19	0·19	0·17	0·19	0·18
H_2O	—	1·8	0·6	0·5	1·5	—	0·6	2·8	3·9	1·3	1·6
CO_2 ppm	—	610	b.d.	b.d.	350	—	b.d.	860	890	b.d.	b.d.
S ppm	1490	1510	60	170	1460	260	390	1400	1420	1440	1440
Cl ppm	720	720	700	640	680	540	1020	910	1060	1060	1060
Olivine (Fo%)	87·4	87·8	87·5	87·5	88·1	88·2	87·0	86·7	87·0	87·1	87·3
% ol added*	9·6	5·3	8·7	6·5	9·1	9·4	6·7	12·3	5	6·2	2·1

Jorullo

	J1d 1	J1d 12_1	J1d 12_2	J1d 12_3	J1d 13_1	J1d 13_2	J1d 14	J1d 17_1	J1d 17_2	J1d 17_A	J1d 20	J1d 23	J1d 24	J1d 28	J1d 29_1	J1d 29_3
SiO_2	51·15	51·54	52·06	51·58	50·60	50·11	50·93	52·90	51·32	51·19	51·22	50·63	49·89	51·57	51·01	50·26
TiO_2	0·79	0·68	0·63	0·75	0·88	0·75	0·67	0·74	0·80	0·74	0·88	0·75	0·73	0·65	0·76	0·71
Al_2O_3	15·66	16·77	17·25	16·96	18·90	19·46	17·15	16·44	17·21	17·46	16·74	17·15	17·87	16·63	17·69	17·55
FeO^T	7·84	7·38	7·30	7·36	7·65	7·26	7·46	7·47	7·52	7·41	7·55	7·56	7·62	7·48	7·65	7·57
MnO	0·15	0·13	0·06	0·08	0·08	0·21	0·02	0·10	0·10	0·04	0·15	0·07	0·05	0·10	0·14	0·09
MgO	10·51	9·23	9·00	9·44	7·75	7·43	9·99	9·29	9·64	9·25	9·91	10·03	10·46	9·82	8·69	9·56
CaO	9·20	9·34	8·57	8·91	8·92	9·21	9·01	8·28	8·55	8·93	9·14	8·96	8·60	8·55	8·92	9·21
Na_2O	3·74	4·13	4·20	4·04	4·26	4·59	3·89	4·01	4·04	4·17	3·60	4·00	3·92	4·25	4·21	4·21
K_2O	0·77	0·65	0·77	0·73	0·81	0·83	0·70	0·65	0·67	0·68	0·61	0·66	0·72	0·84	0·77	0·66
P_2O_5	0·18	0·15	0·16	0·15	0·16	0·16	0·17	0·13	0·15	0·14	0·19	0·19	0·14	0·12	0·16	0·16
H_2O†	1·0	4·4	2·7	4·4	3·3	3·5	1·3	5·7	2·5	2·1	1·6	3·7	2·0	0·9	2·6	2·3
CO_2 ppm†	120	260	220	1020	b.d.	b.d.	320	890	710	b.d.	630	1090	b.d.	b.d.	390	600
S ppm	1150	1200	1380	1450	1590	1560	1720	1750	1670	2070	1850	1880	1780	690	1740	1640
Cl ppm	1100	1180	1200	1240	1290	1410	1380	1240	1310	1290	1270	1200	1190	1110	1180	1210
Olivine (Fo%)	91·1	90·3	89·9	90·4	88·4	88·4	90·5	90·1	90·3	90·1	90·5	90·7	90·6	90·0	89·3	90·2
% ol added*	14·2	6·9	12·4	10·6	3·5	4·4	17·9	9·1	12·5	9·7	11·6	10	20·6	18	8·5	11

(continued)

Table 1: Continued

Cerro el Astillero

	CA-1	CA-2	CA-5	CA-6-1	CA-6-2	CA-7	CA-8	CA-9	CA-10	CA-11	CA-12	CA-12b	CA-14	CA-15
SiO_2	—	53·56	49·67	51·85	—	51·75	—	—	51·50	50·87	50·31	50·64	50·50	50·34
TiO_2	—	0·96	0·91	0·94	—	0·77	—	—	0·83	0·91	0·84	0·88	1·02	0·83
Al_2O_3	—	16·25	17·97	19·02	—	15·41	—	—	17·75	17·94	17·49	16·01	17·88	17·94
FeO^T	—	8·74	8·03	7·98	—	9·58	—	—	8·05	8·09	8·06	8·79	8·10	8·13
MnO	—	0·14	0·10	0·21	—	0·09	—	—	0·14	0·07	0·16	0·08	0·12	0·07
MgO	—	7·04	10·11	8·59	—	9·55	—	—	8·76	8·93	9·49	10·50	8·66	9·28
CaO	—	8·39	8·56	9·00	—	8·37	—	—	9·12	8·88	9·08	7·93	8·98	8·95
Na_2O	—	3·75	3·89	1·63	—	3·72	—	—	3·08	3·55	3·81	4·26	3·95	3·70
K_2O	—	1·01	0·60	0·59	—	0·59	—	—	0·58	0·61	0·60	0·77	0·61	0·61
P_2O_5	—	0·16	0·18	0·18	—	0·17	—	—	0·19	0·16	0·15	0·14	0·19	0·14
H_2O	3·9	1·2	3·1	2·4	2·1	2·6	4·6	2·3	2·9	2·8	3·3	—	4·0	2·8
CO_2 ppm	1210	b.d.	b.d.	220	970	840	1510	520	b.d.	520	610	—	750	430
S ppm	—	400	1513	—	—	1583	—	—	1876	1486	1969	—	1735	1914
Cl ppm	—	1200	1029	—	—	983	—	—	1078	1049	1148	—	986	1059
Olivine (Fo%)	—	87·3	89·3	86·9	—	89·3	—	—	88·8	88·9	89·4	89·4	88·6	89·2
% ol added*	11·7	16·8	18·1	10·2	11·7	16	11·7	11·7	8·9	10·7	8·5	15·5	6·7	9·5

Parícutin

	P506-1	P506-2	P506-3_1	P506-3_2	P506-3_3	P506-4	P506-5	P506-6	P506-7	P506-8	P506-10
SiO_2	52·79	52·81	52·35	—	52·19	53·61	53·22	53·08	53·33	54·19	53·59
TiO_2	0·95	0·94	0·97	—	0·95	1·02	1·01	0·85	0·97	0·91	0·98
Al_2O_3	18·94	18·55	19·09	—	19·29	18·50	19·26	18·42	18·90	19·01	19·24
FeO^T	7·16	7·24	7·21	—	7·13	7·23	7·25	7·15	7·15	7·26	7·02
MnO	0·09	0·07	0·09	—	0·08	0·08	0·07	0·06	0·07	0·15	0·11
MgO	6·52	6·84	6·96	—	6·85	6·51	6·28	6·60	5·98	5·90	5·95
CaO	8·15	8·14	8·04	—	8·04	8·24	8·18	8·36	8·11	7·99	8·34
Na_2O	4·38	4·38	4·26	—	4·43	3·80	3·70	4·45	4·43	3·52	3·73
K_2O	0·80	0·79	0·80	—	0·78	0·80	0·79	0·78	0·81	0·81	0·79
P_2O_5	0·22	0·24	0·25	—	0·26	0·20	0·24	0·25	0·24	0·24	0·23
H_2O	4·5	4·5	3·8	3·4	—	4·2	4·4	4·7	4·1	4·0	4·9
CO_2 ppm	510	1150	850	b.d.	—	720	1020	b.d.	470	870	b.d.
S ppm	1520	1750	1900	—	—	1580	1660	1690	1670	1610	1320
Cl ppm	980	910	940	—	—	930	890	950	950	950	960
Olivine (Fo%)	86·9	87·0	87·4	—	87·4	86·6	86·0	86·9	85·4	86·7	86·1
% ol added*	5·3	10	7·8		7·1	7·7	8·4	9·1	0	3·7	3·3

Cerro San Miguel

	CSM-A_2	CSM-A_3	CSM-A_4	CSM-A_6	CSM-A_7	CSM-A_8	CSM-A_9	CSM-A_10	CSM-A_12	CSM-A_13	CSM-A_14
SiO_2	51·06	57·74	53·69	55·12	55·63	57·24	—	—	51·75	49·81	50·50
TiO_2	0·97	1·19	0·98	1·13	1·24	1·12	—	—	1·10	1·00	1·02
Al_2O_3	20·17	15·88	18·34	19·37	16·37	15·71	—	—	19·38	19·86	18·69
FeO^T	6·64	8·99	6·75	8·55	9·66	10·00	—	—	6·40	6·78	7·09
MnO	0·11	0·15	0·09	0·02	0·11	0·19	—	—	0·11	0·19	0·11
MgO	6·32	4·48	5·69	3·27	5·05	4·16	—	—	6·54	7·25	7·66
CaO	10·12	6·11	9·41	6·65	6·06	6·35	—	—	10·10	10·73	10·46
Na_2O	3·81	3·89	4·17	4·07	4·36	3·78	—	—	3·86	3·71	3·76
K_2O	0·62	1·29	0·66	1·52	1·26	1·23	—	—	0·54	0·50	0·54
P_2O_5	0·20	0·28	0·21	0·31	0·27	0·23	—	—	0·22	0·19	0·16
H_2O	2·6	3·2	4·0	3·7	4·3	3·6	1·2	2·3	1·2	3·6	3·3
CO_2 ppm	1140	640	980	770	720	800	b.d.	b.d.	b.d.	1410	1020
S ppm	2090	1190	1690	1220	1190	1260	—	—	1940	2110	2040
Cl ppm	900	880	880	880	750	900	—	—	900	850	730
Olivine (Fo%)	88·0	75·2	87·2	72·5	75·8	74·1	—	—	88·3	88·6	88·8
% ol added*	1·3	0	0	0	0	0			2	5	4·4

(continued)

Table 1: Continued

Cerro el Pelon

	CeP-1	CeP-2	CeP-3	CeP-7	CeP-8	CeP-9_1	CeP-9_2	CeP-10	CeP-11	CeP-12	CeP-14	CeP-15	CeP-16	CeP-17_1	CeP-17_2	CeP-18
SiO_2	53·84	53·18	—	53·17	52·80	52·42	52·45	52·40	51·80	53·07	53·98	53·89	54·85	53·76	53·41	54·51
TiO_2	1·23	1·29	—	1·16	1·21	1·23	1·11	1·20	1·27	1·25	1·14	1·20	1·04	1·22	1·26	1·31
Al_2O_3	18·62	18·70	—	19·02	19·24	19·23	19·67	19·44	19·54	19·02	18·32	18·62	18·06	19·08	19·07	16·64
FeO^T	7·45	7·55	—	7·52	7·59	7·60	7·45	7·52	7·60	7·51	7·58	7·42	7·57	7·43	7·48	8·43
MnO	0·06	0·02	—	0·02	0·09	0·19	0·05	0·12	0·07	0·20	0·09	0·11	0·13	0·12	0·09	0·13
MgO	5·10	5·68	—	5·31	5·36	5·31	5·24	5·25	5·42	5·17	5·54	4·96	5·32	4·72	4·82	5·73
CaO	8·63	8·16	—	8·55	8·27	8·69	8·69	8·55	8·85	8·45	8·38	8·35	8·17	8·42	8·90	7·49
Na_2O	3·98	4·28	—	4·04	4·23	4·13	4·08	4·33	4·25	4·11	3·75	4·23	3·67	4·03	3·73	4·43
K_2O	0·81	0·80	—	0·89	0·89	0·85	0·90	0·86	0·88	0·90	0·91	0·92	0·88	0·91	0·94	1·03
P_2O_5	0·27	0·33	—	0·33	0·32	0·35	0·35	0·32	0·31	0·31	0·31	0·30	0·33	0·31	0·31	0·30
H_2O	3·7	2·8	2·3	2·3	3·0	1·0	—	2·5	1·6	2·9	2·8	2·8	4·1	2·2	2·3	1·5
CO_2 ppm	710	750	b.d.	b.d.	440	180	—	950	580	650	b.d.	420	b.d.	430	540	b.d.
S ppm	1340	2110	—	1400	1510	1540	1440	1420	1380	1430	1280	1390	560	1310	1490	530
Cl ppm	910	1020	—	1030	960	1040	1040	1010	990	980	920	920	870	990	990	1080
Olivine (Fo%)	83·5	84·5	—	83·9	83·8	83·7	83·7	83·7	84·0	83·4	84·0	81·1	83·8	82·5	82·5	83·2
% ol added*	0	2·2		0	1·3	1·3	2·4	2·4	1·6	1·6	2·8	0	2·8	0·6	2·8	4·2

Cerro La Loma

	CLL-1 in1	CLL-1 in2	CLL-1 in3	CLL-2	CLL-3	CLL-1_2	CLL-1_3	CLL-1_4	CLL-1 5_1	CLL-1 5_2	CLL-1_6	CLL-1_7	CLL-1_8	CLL-1_9	CLL-1_10
SiO_2	53·09	53·45	54·13	52·47	51·62	51·15	52·66	52·66	51·80	51·68	52·79	52·86	54·59	53·33	51·84
TiO_2	1·25	1·25	1·09	0·68	0·89	0·59	1·08	1·08	0·68	0·66	0·70	1·00	1·12	0·99	1·02
Al_2O_3	17·84	18·08	17·55	16·45	15·26	14·81	18·59	18·59	18·72	18·99	18·42	18·88	18·29	18·52	19·16
FeO^T	8·48	8·08	8·03	8·46	8·28	8·78	8·14	8·14	8·20	8·14	8·17	8·20	7·99	7·87	8·84
MnO	0·11	0·15	0·13	0·10	0·13	0·08	0·16	0·16	0·10	0·12	0·09	0·14	0·12	0·16	0·19
MgO	6·13	5·39	5·49	8·02	10·66	11·54	6·19	6·19	6·91	6·85	6·78	5·75	5·16	5·52	5·75
CaO	8·11	8·41	8·45	10·33	9·68	9·44	8·24	8·24	9·74	9·95	10·02	9·02	7·73	9·40	8·97
Na_2O	3·69	3·88	3·79	2·72	2·62	2·77	3·83	3·83	3·22	2·97	2·30	3·36	3·82	3·42	3·44
K_2O	1·07	1·07	1·11	0·68	0·76	0·77	0·91	0·91	0·53	0·55	0·65	0·67	0·94	0·66	0·65
P_2O_5	0·24	0·25	0·23	0·09	0·10	0·07	0·21	0·21	0·10	0·10	0·09	0·14	0·23	0·15	0·14
H_2O	3·2	2·5	3·0	1·3	4·6	3·0	4·2	3·9	4·7	3·2	3·0	2·9	2·5	3·6	3·6
CO_2 ppm	b.d.	b.d.	b.d.	b.d.	2480	1690	1630	1780	2580	2000	980	1190	1040	1490	1250
S ppm	650	680	610	930	950	940	710	780	1630	1080	1960	1010	1010	2020	1870
Cl ppm	620	650	600	1020	1020	1170	630	780	830	960	720	790	660	690	750
Olivine (Fo%)	82·0	82·0	82·0	87·4	90·2	90·3	82·0	80·5	86·1	86·1	86·0	81·8	82·1	82·2	79·7
% ol added*	0	0	0	4	11·2	18·1	0	0	2	1·4	1·1	0	0	0	0

Hoya Alvarez

	HA-A_1	HA-A_1-2	HA-A_2	HA-A_3	HA-A_4	HA-A_6	HA-A_7	HA-A_8	HA-A_10	HA-A_12	HA-A_13-1	HA-A_13-2	HA-A_14	HA-A_15	HA-A_17
SiO_2	46·35	46·60	46·74	45·81	—	47·59	46·17	47·29	48·07	46·98	46·40	46·40	46·96	49·40	47·30
TiO_2	3·21	3·45	2·94	3·16	—	3·18	3·20	2·70	2·98	2·99	2·58	2·52	3·13	2·00	3·04
Al_2O_3	18·19	18·14	17·36	18·46	—	17·81	18·10	17·59	16·72	17·57	17·33	17·46	17·79	16·97	17·41
FeO^T	12·17	12·25	11·10	11·89	—	11·02	11·89	12·01	12·19	12·27	12·32	12·27	12·18	13·01	11·91
MnO	0·14	0·17	0·12	0·16	—	0·18	0·20	0·18	0·15	0·17	0·09	0·13	0·20	0·22	0·21
MgO	4·96	5·03	6·49	5·80	—	5·14	5·52	5·77	5·18	5·31	6·27	6·23	4·91	3·06	3·77
CaO	8·40	8·44	7·81	8·46	—	8·43	8·48	8·02	7·66	8·16	8·56	8·53	8·32	6·54	7·54
Na_2O	4·14	3·44	3·11	3·95	—	4·23	4·19	4·02	4·63	4·10	3·99	4·05	4·10	5·19	4·76
K_2O	1·83	1·86	1·57	1·71	—	1·85	1·70	1·74	1·82	1·86	1·82	1·76	1·80	2·52	2·37
P_2O_5	0·61	0·63	0·59	0·60	—	0·59	0·55	0·57	0·59	0·60	0·63	0·64	0·60	1·11	0·78
H_2O	1·3	1·4	1·1	0·8	1·1	—	0·8	1·1	1·1	1·0	0·8	0·5	1·0	0·4	0·6
CO_2 ppm	3130	6250	b.d.	950	1020	—	1930	2070	1960	2080	2380	2180	2350	1360	1630
S ppm	1180	1150	1040	1120	—	—	1100	950	810	980	950	1010	940	1100	1170
Cl ppm	550	540	410	400	—	—	590	410	540	550	470	390	440	1000	680
Olivine (Fo%)	75·6	75·6	76·8	77·3	—	77·3	77·2	76·3	76·4	78·7	78·7	78·7	74·8	63·6	78·4
% ol added*	2·5	3·6	0	5·4		2·3	4·3	5·2	2·9	3·3	6·6	6·5	2·9	0·3	0

All elements in wt % except for CO_2, S, and Cl. All values have been corrected to be in equilibrium with their olivine host as described in the text. Original (uncorrected) major and trace element data are reported in Electronic Appendix 2. Major elements are normalized to sum to 100% on an anhydrous basis. Volatile concentrations are not normalized. For inclusions analyzed only by FTIR, H_2O and CO_2 were corrected using the average per cent olivine added for that cone. b.d., below detection limit; —, not determined.

*Amount of olivine added back to melt inclusion composition to correct for post-entrapment crystallization.

†The H_2O and CO_2 values reported here are slightly higher than those reported by Johnson *et al.* (2008) because here we used room temperature glass densities that varied as a function of dissolved H_2O, whereas Johnson *et al.* (2008) used a constant density for all inclusions.

Table 2: Trace element data (corrected for post-entrapment crystallization and Fe loss) from LA ICP-MS analyses of melt inclusions

Cone	Inclusion	Rb	Ba	Th	U	Nb	Ta	La	Pb	Ce	Sr	Nd	Zr	Sm	Eu	Ti	Dy	Y	Yb
San Juan	CSJ-5_2	16·2	364	1·74	0·40	15·7	1·31	17·2	4·77	38·7	587	22·8	156	3·57	1·63	7323	3·30	24·9	1·75
San Juan	CSJ-32	18·0	315	1·18	0·30	13·6	0·63	13·6	5·02	33·1	451	15·9	109	3·07	1·26	6286	3·34	16·4	1·51
San Juan	CSJ-33	15·2	345	1·17	0·57	15·1	0·70	17·0	4·33	36·7	528	18·0	120	3·83	0·97	7038	2·73	18·8	2·03
Hungaro	CeH-15	8·8	275	0·56	0·24	4·8	0·28	11·7	4·72	23·3	551	10·3	99	2·16	1·03	5063	2·97	13·7	2·19
Hungaro	CeH-24b	11·0	311	0·50	0·28	5·0	0·31	10·3	4·72	25·7	491	13·1	85	2·77	0·92	5478	1·80	11·4	1·30
Hungaro	CeH-88	9·3	274	0·49	0·30	5·1	0·21	9·5	4·24	23·6	502	13·3	85	1·79	0·85	4578	2·34	11·3	0·62
Jorullo	J1d-12_3	8·9	197	0·34	0·08	2·3	0·15	7·2	3·49	15·7	470	12·1	72	6·02	1·20	4109	2·32	15·3	2·08
Jorullo	J1d-20	6·7	185	b.d.l.	b.d.l.	1·9	b.d.l.	6·4	3·96	16·4	467	8·9	70	2·37	1·17	3929	2·11	13·5	1·13
Jorullo	J1d-24	6·2	167	0·46	b.d.l.	1·9	b.d.l.	6·2	8·88	11·8	408	8·4	70	1·33	0·65	3199	3·19	11·8	1·31
Jorullo	J1d-28	10·5	237	0·68	0·17	2·9	b.d.l.	8·1	3·71	17·1	435	13·7	85	0·93	0·84	4091	2·58	17·1	1·78
Astillero	CA-A_12-2	4·2	143	0·29	0·14	2·4	0·10	5·5	2·19	13·2	385	9·0	49	2·16	0·75	3926	1·76	9·5	0·99
Astillero	CA-A 14	5·9	184	0·47	0·17	3·5	0·15	6·6	2·95	17·0	485	10·1	61	2·60	0·88	4985	2·30	12·9	1·56
Astillero	CA-A_15	5·9	193	0·41	0·11	3·1	0·10	6·7	3·27	17·1	487	10·2	57	2·30	0·76	4943	1·98	12·0	0·63
Parícutin	P506-3_1	7·5	218	0·65	0·22	4·6	0·24	8·1	4·45	20·1	580	11·2	77	2·49	0·99	5200	2·39	12·7	0·82
Parícutin	P506-6	8·8	225	0·72	0·29	4·0	0·22	8·2	4·95	21·1	582	11·6	69	2·89	0·86	5278	2·30	11·9	1·15
Parícutin	P506-10	8·3	246	0·66	0·24	4·8	0·31	9·3	3·56	23·2	609	11·4	77	3·39	0·91	5495	2·20	12·8	0·90
San Miguel	CSM-A-12	6·9	180	0·58	b.d.l.	4·3	0·18	7·8	2·88	21·3	470	10·8	78	4·67	0·85	6153	2·43	16·0	1·62
San Miguel	CSM-A 13	6·1	169	0·55	0·10	4·0	0·15	7·9	3·16	19·1	477	11·8	85	2·59	1·06	6113	3·56	18·7	1·93
San Miguel	CSM-A-14	5·6	178	0·53	0·17	3·9	0·18	6·9	2·87	19·7	450	9·9	74	2·19	1·01	5896	2·53	14·9	1·50
El Pelon	CeP-2	16·6	399	1·26	0·55	8·0	0·31	15·1	4·71	36·6	900	21·2	135	4·10	1·33	6839	3·23	18·8	1·39
El Pelon	CeP-7	19·6	306	1·58	0·59	8·7	0·57	15·4	5·12	40·1	921	16·8	127	3·42	1·25	7204	3·03	16·8	1·59
El Pelon	CeP-11	18·7	301	1·39	0·60	9·3	0·52	16·0	5·39	41·7	938	17·8	124	3·04	1·39	7415	2·57	16·7	2·08
El Pelon	CeP-18	20·1	344	1·69	0·60	8·8	0·31	17·8	5·88	42·1	711	22·0	136	3·41	1·51	6978	3·40	21·3	1·57
La Loma	CLL-1-2	6·2	100	0·59	0·22	2·2	0·12	3·8	2·07	9·9	449	5·9	38	1·05	0·58	3249	1·33	7·8	0·73
La Loma	CLL-1-6	8·8	139	0·97	0·25	2·7	0·22	5·0	2·98	12·5	538	8·0	56	1·60	0·71	4168	2·08	11·6	1·56
La Loma	CLL-1-7	10·5	187	1·06	0·36	4·8	0·26	7·3	3·56	18·1	651	10·8	68	2·43	1·24	5812	2·33	13·3	1·25
La Loma	CLL-1-9	13·0	188	1·09	0·49	4·6	0·30	7·7	4·01	19·3	619	10·5	78	2·74	1·12	6233	2·03	15·4	1·48
Hoya Alvarez	HA-A-13_1	21·2	295	3·41	1·09	46·8	3·01	31·5	2·76	61·4	700	29·1	211	5·35	1·77	14928	4·82	26·0	1·82
Hoya Alvarez	HA-A-13_2	18·5	270	3·24	0·92	46·3	2·36	30·0	2·40	58·4	661	27·4	195	7·69	1·68	14183	3·79	23·8	2·08

b.d.l., below detection limit. Original values (uncorrected) are reported in Electronic Appendix 3.

Table 3: Average oxygen isotope compositions of olivine

	$\delta^{18}O_{olivine}$	±1σ
San Juan	5·79	0·08
Hungaro	6·03	0·08
Jorullo	5·62	0·13
Astillero	5·94	0·16
Parícutin*	5·92	
San Miguel	5·65	0·08
El Pelon	5·98	0·10
La Loma	5·83	0·08
Hoya Alvarez	5·48	0·15

*Single analysis.

CO_2, whereas melt inclusions at Hoya Alvarez trapped melts with ≤1·4 wt % H_2O and ≤6200 ppm CO_2 (all values are from Table 1 and are corrected for post-entrapment crystallization and Fe loss). In contrast, S and Cl concentrations show much less variability (Table 1). The highly variable H_2O and CO_2 contents for inclusions from a given cone are the result of degassing during ascent and crystallization caused by the pressure-dependent solubilities of these components, though the details of degassing processes are complex and poorly understood (Johnson *et al.*, 2008, 2009; Métrich & Wallace, 2008; Vigouroux *et al.*, 2008). Thus, the highest H_2O and CO_2 melts trapped within inclusions at a given volcano most closely represent the initial melt volatile contents (or at least provide a minimum value). However,
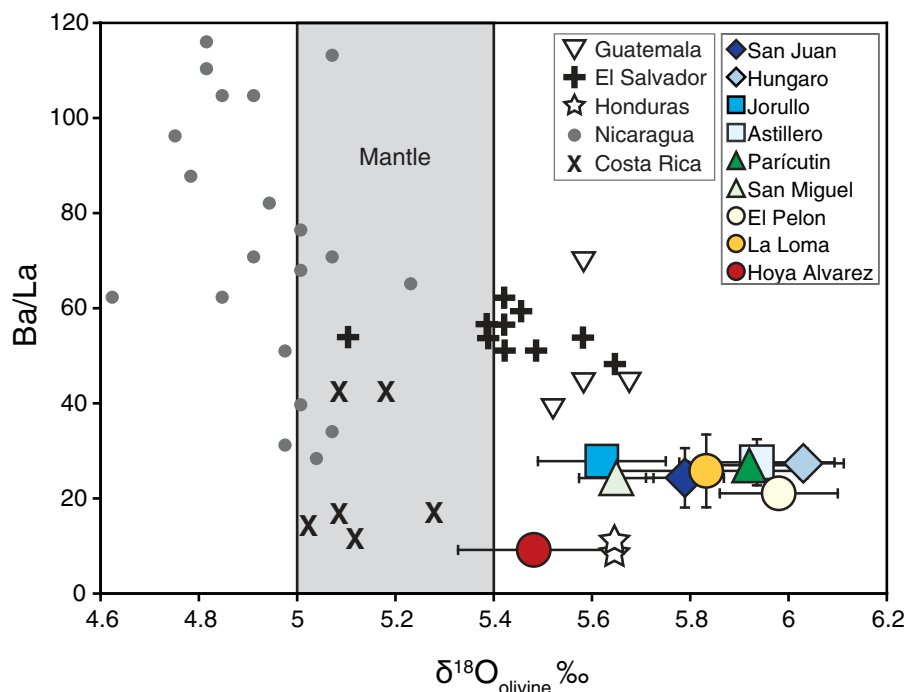
Fig. 3. Ba/La vs olivine oxygen isotope composition for Central America (Eiler *et al.*, 2005; whole-rock Ba/La values) and Mexico (this study; melt inclusion Ba/La values; Table 4).

because of the low solubility of CO_2, melt inclusions probably never trap melts with CO_2 values close to initial magmatic values (Wallace, 2005), and therefore estimates of initial CO_2 cannot be made with the melt inclusion data. The maximum H_2O concentrations measured in melt inclusions across the MGVF are similar to H_2O concentrations documented for least-degassed melt inclusions from other arc volcanoes in Central America (e.g. Roggensack *et al.*, 1997; Walker *et al.*, 2003; Wade *et al.*, 2006; Benjamin *et al.*, 2007), and further to the east in Mexico in the Chichináutzin Volcanic Field (Cervantes & Wallace, 2003). We also assume that the highest measured S and Cl concentrations for melt inclusions from each volcano are closest to initial melt concentrations, although these data show less variability than H_2O and CO_2 because Cl and S have higher solubilities during degassing (e.g. Spilliaert *et al.*, 2006).

Oxygen isotope compositions of olivine

MGVF olivine have $\delta^{18}O_{olivine}$ values ranging from $5 \cdot 5 \pm 0 \cdot 2‰$ to $6 \cdot 0 \pm 0 \cdot 1‰$ (Table 3), which are high in comparison with olivine in mantle peridotites ($5 \cdot 2 \pm 0 \cdot 2‰$; Mattey *et al.*, 1994; Eiler, 2001). Most arc basalts around the world have $\delta^{18}O_{olivine} = 5 \cdot 2 \pm 0 \cdot 2‰$ (Eiler *et al.*, 2000; Eiler, 2001), identical to the range for mantle olivine. However, there are a few arcs where lower values (4·6–4·9‰, Nicaragua; Eiler *et al.*, 2005) and higher values have been found ($\leq 5 \cdot 7‰$ for Central America; Eiler *et al.*,

2005; $\leq 7 \cdot 2‰$ in Kamchatka; Dorendorf *et al.*, 2000; Bindeman *et al.*, 2004, 2005; Auer *et al.*, 2009; <6·3‰ for Mt. Shasta, Cascade arc; Martin *et al.*, 2009). The high $\delta^{18}O_{olivine}$ values found in the MGVF are higher than in olivine from most arc basalts from Central America (Fig. 3). Interestingly, the MGVF data extend the observed northward trend of increasing $\delta^{18}O_{olivine}$ values and decreasing Ba/La from Nicaragua to Guatemala (Eiler *et al.*, 2005). Compared with the alkali basalt sample from Hoya Alvarez, the calc-alkaline samples have higher $\delta^{18}O_{olivine}$ values and higher concentrations of elements that are likely to be mobilized from the subducted slab (Fig. 4). There is no correlation of oxygen isotope values with distance from the trench (Fig. 5d).

DISCUSSION
Primary melt compositions and across-arc variations

To compare volatile contents and melt compositions across the MGVF, primary melt compositions [i.e. melts that would be in equilibrium with mantle olivine (Fo_{90})] were calculated for each volcano in this study. Two of the cinder cones erupted tephra with Fo_{90-91} olivine, and thus the compositions of their melt inclusions were considered primary melts. Melt inclusions in samples with lower-Fo olivine were corrected by adding olivine back into each melt inclusion composition until it reached equilibrium
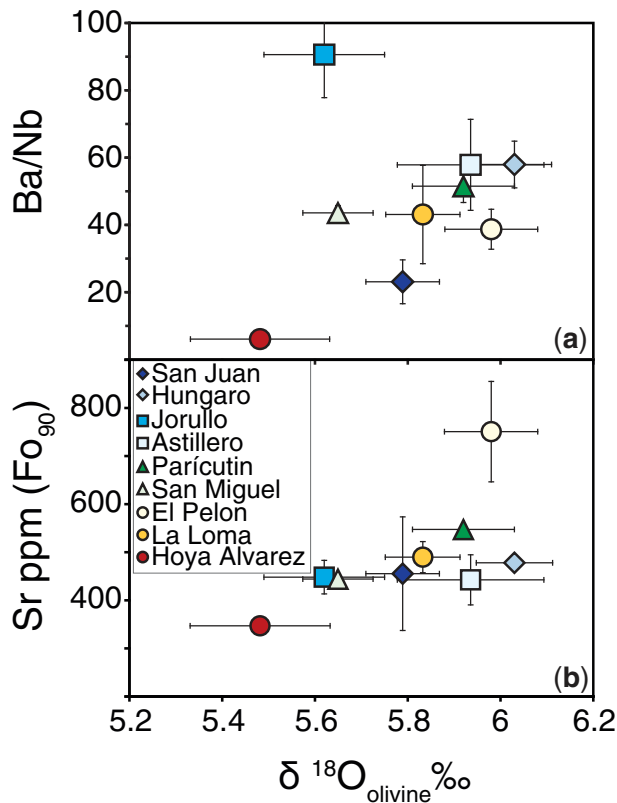
Fig. 4. Melt inclusion Ba/Nb and Sr vs oxygen isotope composition of olivine. The Sr data are for melts in equilibrium with Fo$_{90}$ olivine (Table 4).

with Fo$_{90}$ olivine. This correction involved addition of ≤14 wt % olivine.

Hoya Alvarez melt inclusions are more evolved than those from the other volcanoes. Correcting these melts to Fo$_{90}$ by olivine addition only would yield erroneous results because the Hoya Alvarez tephra contains large crystals of olivine, plagioclase, and clinopyroxene, and the low MgO of the melt inclusions makes it likely that the melt compositions were affected by multiphase fractionation. Because of these complexities, we modeled the fractionation paths of a melt with similar composition (i.e. alkali basalt) that was in equilibrium with Fo$_{90}$ olivine. We found that an alkali basalt from the Rio Grande Rift, New Mexico (McMillan *et al.*, 2000), when fractionated via isobaric crystallization in MELTS (Ghiorso & Sack, 1995), produced the melt compositions erupted at Hoya Alvarez by fractionation of 23% olivine, 20% plagioclase, and 6% clinopyroxene (a total of 49% fractionation). Therefore, we corrected the volatile and trace element compositions at Hoya Alvarez for 49% fractionation, and we assumed that the major element composition of the primary melt resembled that of the Rio Grande basalt, which has 11 wt % MgO.

In all subsequent figures and discussion, we present melt compositions and volatile concentrations that represent the primary mantle melts in equilibrium with Fo$_{90}$. Calculated primary melt compositions are given in Table 4.

Major and trace elements

The heterogeneity of incompatible trace element abundances in calculated MGVF primary melts is shown in Fig. 6. Most primary melts have enrichments in large ion lithophile elements (LILE) and depletions in Nb and Ta, a pattern typical of subduction-related magmas. Elements that are strongly partitioned into fluids or hydrous melts released from altered oceanic crust and/or subducted sediment (e.g. Ba, Pb, Sr; Kessel *et al.*, 2005) are variably enriched. Additionally, there are large variations in the degree of Nb and Ta depletion relative to elements of similar incompatibility. Basalts with no Nb–Ta depletion in the MGVF and elsewhere in the TMVB are typically transitional to alkalic in composition, like Hoya Alvarez, and have been referred to either as ocean island basalt (OIB) or intraplate-type alkaline basalts (Luhr *et al.*, 1989; Luhr, 1997; Wallace & Carmichael, 1999).

The MGVF primary melts display no systematic across-arc variations in major or trace element compositions or key trace element ratios, apart from the fact that the alkali basalt volcanic center farthest behind the volcanic front (Hoya Alvarez) is distinctly different in composition from all others (Fig. 5). Primary melt Nb/Y ratios plot mostly between normal mid-ocean ridge basalt (N-MORB) and enriched (E)-MORB values. Ba/La ratios are low compared with other arcs. Magmas in the Aleutian arc have Ba/La ratios of 20–50 (Singer *et al.*, 2007), and much higher values occur in Central America (≤100; Eiler *et al.*, 2005). However, values for the MGVF calc-alkaline melts are elevated compared with average N-MORB (2·5) and E-MORB [9·0; values from Sun & McDonough (1989)]. Ba/Nb and Dy/Yb ratios for the calc-alkaline samples are also higher than MORB values. In contrast to the calc-alkaline samples, Hoya Alvarez has lower Ba/La and Ba/Nb and higher Nb/Y and Dy/Yb ratios that are similar to OIB values. The primitive melt from San Juan has Nb/Y and Ba/Nb that are intermediate between the values for the other calc-alkaline samples and the Hoya Alvarez alkali basalt.

Volatiles

The H$_2$O, Cl, and S concentrations in primary melts (i.e. maximum melt inclusion values for each volcano recalculated for melts in equilibrium with Fo$_{90}$, where necessary) from the calc-alkaline samples are high (2·5–5·75 wt % H$_2$O, 700–1350 ppm Cl, 1100–2000 ppm S) for large distances (~150 km) across the arc (Fig. 7). In contrast, the Hoya Alvarez alkali basalt has low volatile contents. San Juan, although calc-alkaline in composition, has volatile contents that are intermediate between Hoya Alvarez and
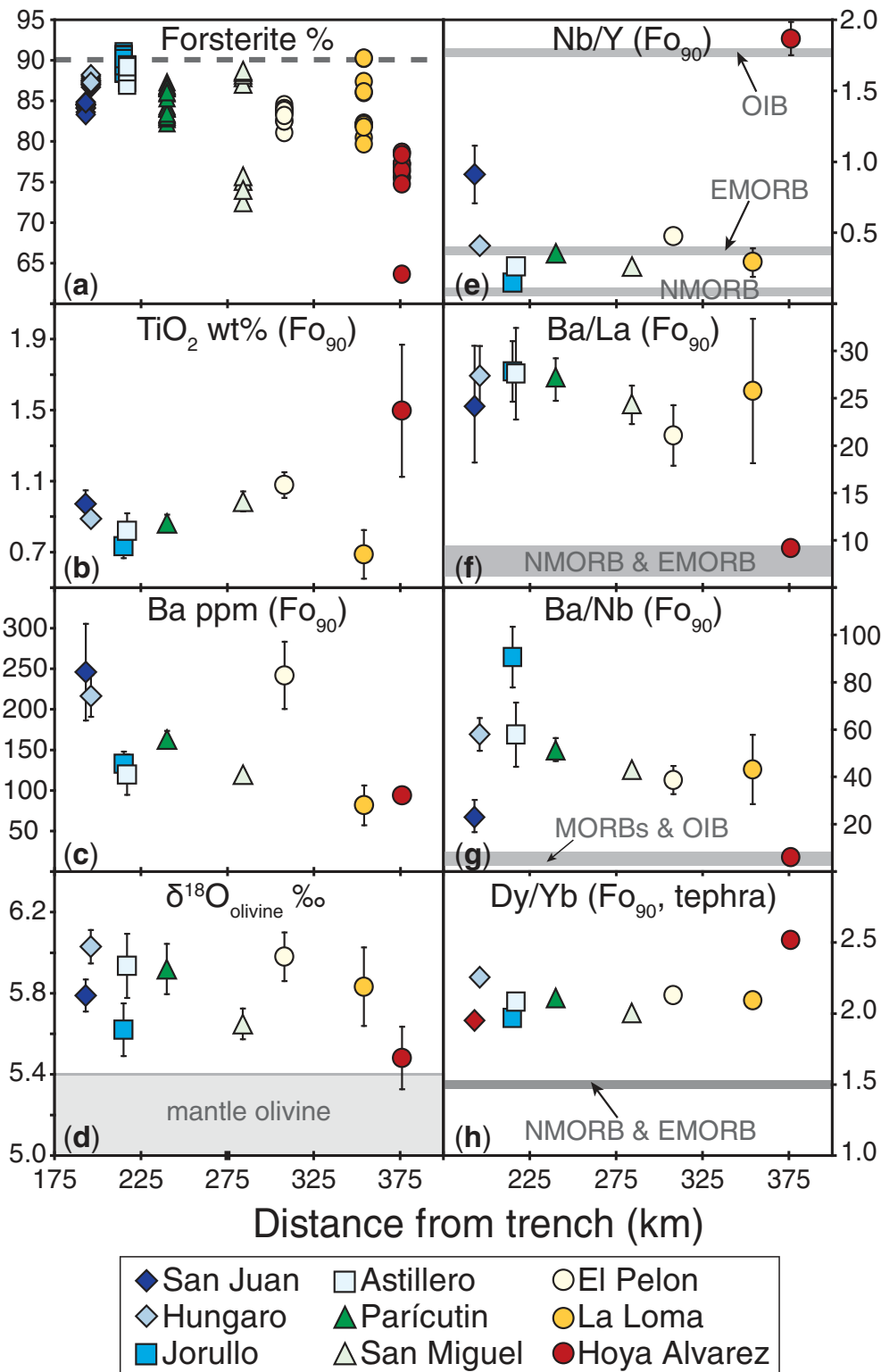
Fig. 5. Across-arc variations in olivine and melt inclusion compositions. In this and subsequent figures, primary melt values refer to melts recalculated to be in equilibrium with Fo_{90} olivine (Table 4). Dy/Yb ratios in (h) are from bulk tephra ICP-MS analyses. Shown for comparison are N-MORB, E-MORB and OIB average values from Sun & McDonough (1989).

Table 4: Primitive melt compositions (in equilibrium with Fo$_{90}$ olivine) calculated from melt inclusion data

	San Juan	Hungaro	Jorullo	Astillero	Parícutin	San Miguel	El Pelon	La Loma	Hoya Alvarez*
SiO$_2$ wt %	49·9 ± 0·5	52·8 ± 0·7	51·2 ± 0·8	50·3 ± 0·5	52·2 ± 0·5	50·4 ± 0·7	51·6 ± 0·8	51·5 ± 0·3	45·2
TiO$_2$	0·97 ± 0·08	0·89 ± 0·03	0·73 ± 0·07	0·82 ± 0·10	0·86 ± 0·05	0·99 ± 0·06	1·08 ± 0·07	0·69 ± 0·14	2·0
Al$_2$O$_3$	15·6 ± 0·7	17·1 ± 0·1	17·0 ± 0·6	16·9 ± 1·4	17·6 ± 0·3	18·8 ± 0·5	16·8 ± 0·4	15·5 ± 0·8	14·3
FeO^T	9·6 ± 0·2	7·7 ± 0·2	7·5 ± 0·1	8·5 ± 0·7	7·5 ± 0·1	6·9 ± 0·3	8·1 ± 0·0	8·5 ± 0·2	11·0
MnO	0·08 ± 0·02	0·08 ± 0·01	0·09 ± 0·04	0·10 ± 0·03	0·09 ± 0·03	0·13 ± 0·04	0·04 ± 0·03	0·10 ± 0·03	0·17
MgO	12·5 ± 0·9	9·5 ± 0·3	9·7 ± 0·5	10·4 ± 0·9	9·3 ± 0·2	8·4 ± 0·3	10·2 ± 0·1	10·9 ± 0·5	11·3
CaO	7·3 ± 0·3	7·6 ± 0·2	8·9 ± 0·3	8·6 ± 0·4	7·6 ± 0·2	10·0 ± 0·4	7·5 ± 0·2	9·5 ± 0·3	9·0
Na$_2$O	3·1 ± 0·2	3·4 ± 0·8	4·0 ± 0·2	3·7 ± 0·2	3·9 ± 0·4	3·6 ± 0·1	3·6 ± 0·2	2·5 ± 0·3	2·6
K$_2$O	0·79 ± 0·07	0·74 ± 0·12	0·70 ± 0·06	0·59 ± 0·02	0·74 ± 0·01	0·53 ± 0·04	0·77 ± 0·04	0·69 ± 0·09	0·91
P$_2$O$_5$	0·20 ± 0·01	0·20 ± 0·03	0·16 ± 0·02	0·16 ± 0·02	0·22 ± 0·01	0·18 ± 0·02	0·28 ± 0·01	0·08 ± 0·01	0·36
H$_2$O†	2·4 ± 0·2	3·8 ± 0·4	5·7 ± 0·8	3·8 ± 0·3	4·5 ± 0·4	3·7 ± 0·3	3·6 ± 0·3	4·6 ± 0·5	0·7 ± 0·1
Cl ppm†	713 ± 90	988 ± 93	1338 ± 65	1138 ± 150	913 ± 80	904 ± 19	913 ± 94	1024 ± 70	263 ± 67
S ppm†	1055 ± 36	1431 ± 131	2066 ± 57	1953 ± 132	1791 ± 51	2046 ± 69	1861 ± 117	1763 ± 141	578 ± 74
Rb ppm	14·2 ± 2·1	9·0 ± 1·3	7·3 ± 1·5	5·2 ± 0·9	7·6 ± 0·5	6·0 ± 0·9	16·2 ± 1·1	8·3 ± 1·8	10·1 ± 1·0
Ba	296 ± 60	267 ± 26	183 ± 14·9	170 ± 25	213 ± 10	173 ± 1	292 ± 41	132 ± 25	144 ± 9
U	0·36 ± 0·11	0·26 ± 0·04	0·13 ± 0·06	0·14 ± 0·03	0·23 ± 0·03	0·17 ± 0·05	0·51 ± 0·02	0·28 ± 0·09	0·51 ± 0·06
Th	1·20 ± 0·47	0·48 ± 0·01	0·40 ± 0·08	0·38 ± 0·09	0·63 ± 0·03	0·54 ± 0·03	1·27 ± 0·14	0·80 ± 0·14	1·70 ± 0·06
Nb	12·8 ± 2·5	4·6 ± 0·3	2·0 ± 0·2	2·9 ± 0·5	4·1 ± 0·3	4·0 ± 0·2	7·5 ± 0·4	3·1 ± 0·9	23·7 ± 0·2
Ta	0·79 ± 0·45	0·25 ± 0·05	0·15 ± -	0·11 ± 0·03	0·24 ± 0·04	0·18 ± 0·00	0·37 ± 0·12	0·19 ± 0·05	1·37 ± 0·23
La	12·2 ± 1·9	9·7 ± 0·6	6·6 ± 0·5	6·1 ± 0·6	7·9 ± 0·5	7·1 ± 0·6	13·9 ± 0·7	5·1 ± 1·2	15·7 ± 0·5
Pb	3·7 ± 0·7	4·2 ± 0·2	3·7 ± 0·3	2·7 ± 0·5	4·0 ± 0·7	2·8 ± 0·0	4·6 ± 0·3	2·7 ± 0·5	1·3 ± 0·1
Ce	31 ± 6	23 ± 2	15 ± 2	15 ± 2	20 ± 1	20 ± 1	35 ± 2	13 ± 3	31 ± 1
Sr	455 ± 118	478 ± 11	448 ± 35	443 ± 52	547 ± 8	444 ± 11	751 ± 104	490 ± 32	347 ± 14
Nd	16·6 ± 5·4	11·4 ± 2·0	9·8 ± 2·0	9·6 ± 0·5	10·6 ± 0·2	10·0 ± 0·6	16·8 ± 2·1	7·6 ± 1·3	14·4 ± 0·6
Zr	91 ± 6	83 ± 4	71 ± 1	54 ± 5	69 ± 4	73 ± 2	113 ± 5	52 ± 10	104 ± 6
Sm	3·0 ± 0·6	2·1 ± 0·5	2·0 ± 0·6	2·3 ± 0·2	2·7 ± 0·4	3·3 ± 1·7	3·0 ± 0·4	1·7 ± 0·5	2·4 ± 0·3
Ti	5979 ± 1205	4685 ± 438	3746 ± 482	4518 ± 533	4938 ± 74	5822 ± 139	6141 ± 264	4185 ± 838	7423 ± 269
Dy‡	2·7 ± 0·6	2·5 ± 0·2	2·5 ± 0·4	2·0 ± 0·2	2·2 ± 0·1	2·4 ± 0·1	2·6 ± 0·3	1·9 ± 0·2	2·5 ±
Y	14 ± 1	11 ± 1	14 ± 2	11 ± 2	12 ± 0	15 ± 1	16 ± 2	10 ± 2	13 ± 1
Yb‡	1·4 ± 0·3	1·1 ± 0·5	1·3 ± 0·2	1·1 ± 0·4	1·0 ± 0·2	1·5 ± 0·1	1·4 ± 0·3	1·0 ± 0·2	1·1 ±

Major elements in wt %; Cl, S and trace elements in ppm. These data represent the average primary melt compositions, errors represent 1 SD based on the average of 2–4 samples. The melt inclusion data from which these values were calculated are given in Table 1 (major element corrected values) and Electronic Appendix 2 (uncorrected major element values), and corrected trace element values are given in Table 2 (uncorrected trace element analyses are reported in Electronic Appendix 3). (See text for details.) Trace elements are calculated from average of Hoya Alvarez melt inclusions corrected for 49% crystallization. H$_2$O, Cl and S are calculated from maximum values in Hoya Alvarez melt inclusions.
*Major element composition of alkali basalt from McMillan *et al.* (2000), which produces the Hoya Alvarez average melt inclusion composition by 49% fractional crystallization.
†Values for H$_2$O, Cl, and S were calculated from the maximum values found in melt inclusions from each cone.

the other calc-alkaline cones, similar to its intermediate Nb/Y and Ba/Nb ratios described above (see Fig. 5). The persistently high volatile contents of the MGVF primary calc-alkaline melts differ from previous across-arc studies. In Guatemala, measured H$_2$O values are variable but highest (<6 wt %) in the volcanic front and decrease rapidly (within <80 km) to values of ∼2 wt % behind the front (Walker *et al.*, 2003). An across-arc study of

Kamchatka showed moderate melt H$_2$O contents (∼2–2·5 wt %) that are fairly constant across the arc (Portnyagin *et al.*, 2007).

Importantly, the ratio of maximum Cl to H$_2$O for each cone is relatively constant across the MGVF (Figs 7e and 8). The Cl/H$_2$O ratio corresponds to a NaCl equivalent of ∼4 wt %, which is close to the salinity of seawater (∼3·5 wt %) and similar to values for some other arcs
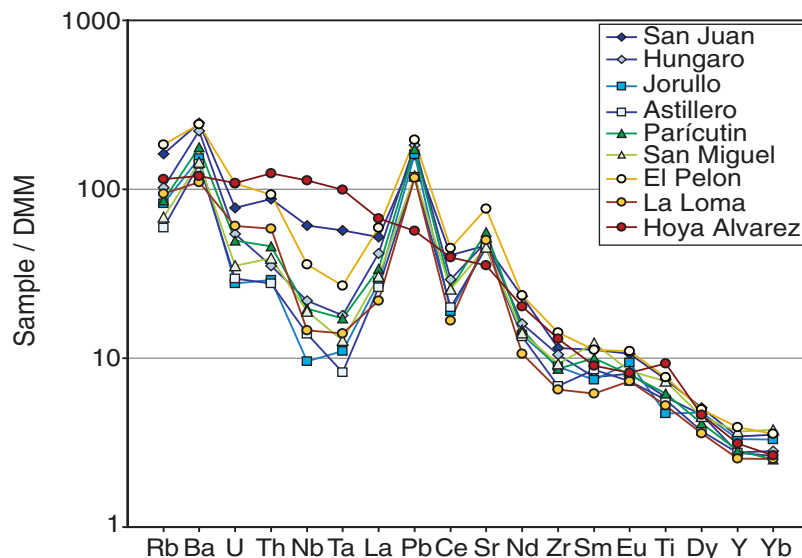
Fig. 6. Trace elements in primary MGVF melts (Table 4) normalized to depleted MORB mantle (DMM; from Salters & Stracke, 2004). Diamonds and squares represent those volcanoes along or near the volcanic front, triangles are those between 50 and 100 km from the front, and circles are those >100 km from the front (see Fig. 2).

(Fig. 8). The relatively constant Cl/H_2O ratios lend added support to the use of the maximum melt inclusion H_2O contents measured at each volcano, because melt H_2O contents can be strongly affected by degassing but Cl contents show minimal degassing effects (Johnson *et al.*, 2009). Although H_2O values at each cone show variable effects of degassing during magma ascent, the maximum melt inclusion H_2O values measured must be close to the initial melt H_2O concentrations for the Cl/H_2O ratio to be constant. Primary melt S/Cl ratios show a systematic increase with distance from the trench from the volcanic front to ~100 km behind the front (Fig. 7f). A similar pattern and comparable S/Cl ratios were found in Kamchatka (Portnyagin *et al.*, 2007).

The ratio of H_2O to Ce is a useful indicator of mantle enrichment in H_2O because H_2O and Ce have similar incompatibility during melting of spinel lherzolite, although H_2O becomes less incompatible than Ce in garnet lherzolite (Hauri *et al.*, 2006). For the MGVF primary melts, the variation of H_2O/Ce with distance from the trench generally mimics the pattern for H_2O (Fig. 7d), and all $H_2O/$ Ce values except for Hoya Alvarez are higher than N-MORB to E-MORB values (e.g. 140–250; le Roux *et al.*, 2006). For all MGVF primary melts, there is a strong positive correlation of H_2O/Ce with Ba/Nb, which demonstrates that enrichment of LILE relative to high field strength elements (HFSE) is directly linked to addition of hydrous fluids or melts from the subducted slab into the mantle wedge (Fig. 9a). The negative correlation of H_2O with TiO_2 (Fig. 9b) shows that more depleted mantle source regions receive a larger amount of the hydrous

subduction component (e.g. Cervantes & Wallace, 2003) and/or that variations in the amount of hydrous component added produce large differences in degrees of melting (e.g. Stolper & Newman, 1994).

Estimating magmatic H_2O for other cones in the MGVF and central Mexico

In this study we sampled nine of the ~900 cinder cones in the MGVF (Hasenaka & Carmichael, 1985). To assess broader patterns in H_2O, correlations between H_2O and trace elements in the melt inclusion data were used to estimate H_2O contents for cinder cones in the surrounding MGVF for which there are published geochemical data. The calibrated relationship between H_2O and incompatible trace elements can also be applied to data from cinder cones to the east of the MGVF in the Zitácuaro–Valle de Bravo (ZVB) and Chichináutzin volcanic fields (CVF). Ratios of Sr (fluid mobile) to other incompatible elements (Nb, La, Ti) in the MGVF melt inclusions correlate strongly with melt inclusion H_2O contents (Fig. 10), and previously analyzed melt inclusions from the CVF (Cervantes & Wallace, 2003) show a similar relationship. Using the linear regressions for these correlations, H_2O contents were calculated for other cinder cones in the MGVF, ZVB, and CVF for which whole-rock trace element data are available. The available data were filtered to include only compositions similar to those in this study; thus the data were limited to calc-alkaline basalts and basaltic andesites and transitional to alkalic basalts similar to the Hoya Alvarez composition. Because some datasets did not have reliable Nb data, the correlation involving Nb was
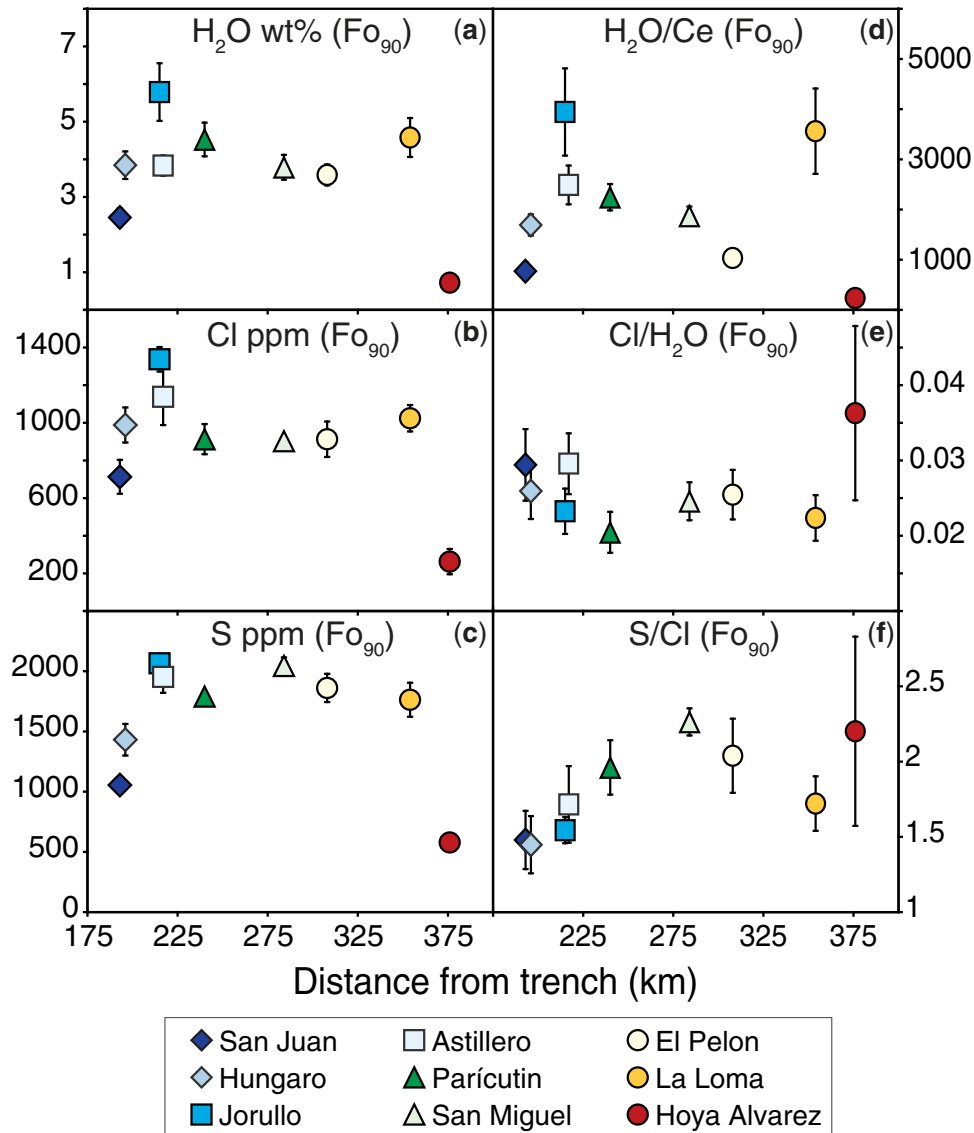
Fig. 7. Volatile contents of primary melts vs distance from the trench. For each cone, the plotted value represents the highest measured volatile concentration in melt inclusions recalculated for a melt in equilibrium with Fo_{90} olivine (Table 4). Error bars show $\pm 1\sigma$ values based on replicate analyses of the inclusion from each cone with the highest volatile content. For (d), the error bars shown for H_2O/Ce include the $\pm 1\sigma$ uncertainty in average Ce for all inclusions from a given cone. In general, maximum H_2O, Cl, and S remain high for large distances (<150 km) behind the volcanic front.

not always used. The error in these calibrations was assessed by back-calculating H_2O contents for the MGVF melt inclusions in this study and those from the CVF that were used in the calibration. We found that the calibration reproduced the measured H_2O values in the MGVF and CVF with a root mean squared error (r.m.s.e.) of ± 1.4 wt % H_2O.

We calculated H_2O contents for 269 monogenetic volcanoes in the MGVF and the central TMVB and produced a map of magmatic H_2O across central Mexico (Fig. 11). The map shows high H_2O (4–6 wt %) along the volcanic front in the MGVF and a striking broad region of

moderately high H_2O ($>\sim 3$ wt %) continuing over a large region behind the volcanic front. Far behind the front (~ 175 km) the data display an abrupt decrease in melt H_2O, with a large region of consistently lower H_2O contents (<3 wt %). To test how representative the nine cones sampled for this study are of the broader field, we plotted the measured melt inclusion maximum H_2O contents and the calculated H_2O contents against distance from the trench (Fig. 12). Although there is significant scatter in the MGVF calculated H_2O contents, the nine samples from this study are broadly representative of the spatial variability in H_2O contents across the arc,
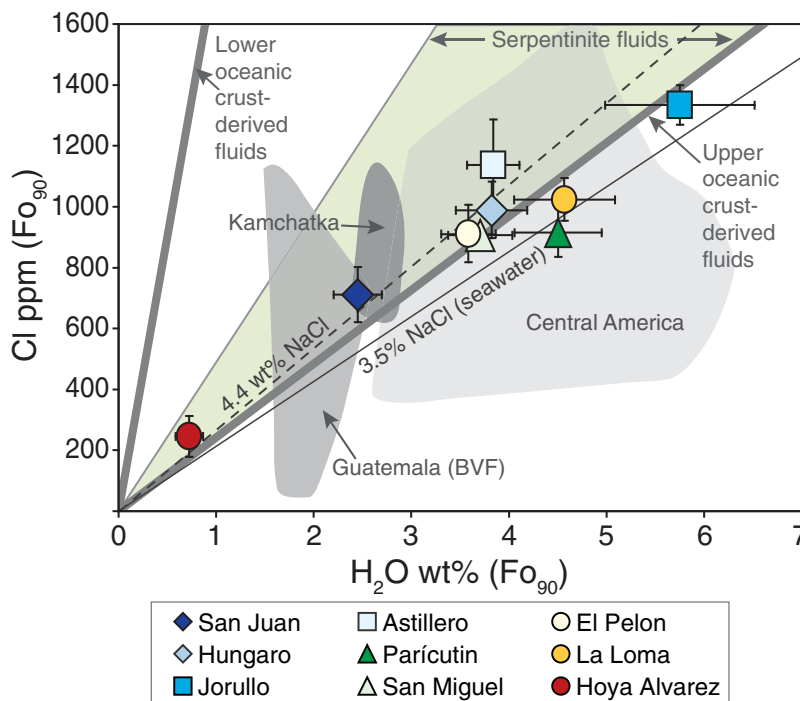
Fig. 8. Covariations in primary melt Cl and H_2O contents for each volcano. The correlation shown in this plot is not caused by degassing because only data for the least-degassed inclusion from each cone are used. The data fall along a line of relatively constant salinity (4·4 wt % NaCl; after Kent *et al.*, 2002). Also shown are the ranges of salinities for typical serpentinite-derived fluids (Scambelluri *et al.*, 2004), oceanic crust-derived fluids (wide gray lines; Philippot *et al.*, 1998), and seawater. The MGVF data are broadly similar to data from Central America [Roggensack *et al.*, 1997; Roggensack, 2001; Guatamala behind the volcanic front (BVF) data from Walker *et al.*, 2003] and the Kamchatka arc (Portnyagin *et al.*, 2007).
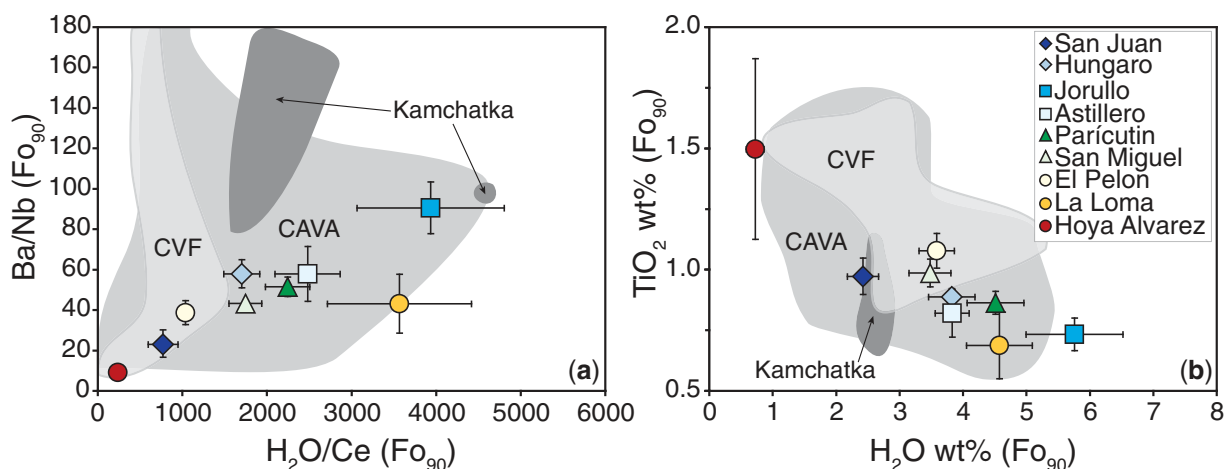
Fig. 9. Comparison of H_2O and H_2O/Ce in MGVF melt inclusions with data from the Chichináutzin Volcanic Field, Mexico (CVF; Cervantes & Wallace, 2003), Central American volcanic arc (CAVA; Roggensack *et al.*, 1997; Roggensack, 2001; Walker *et al.*, 2003; Wade *et al.*, 2006; Sadofsky *et al.*, 2008) and Kamchatka (Portnyagin *et al.*, 2007).

including the wide range of H_2O contents (from moderate to low) in the region farthest behind the front.

Spatial variations in magmatic H_2O to the east of the MGVF show different patterns. In the ZVB, the calculated H_2O values are high at the volcanic front (~5–6 wt %), but unlike the MGVF, the melt H_2O contents decrease systematically with distance behind the front (to the NNW). Further to the east in the CVF the data are more sparse,
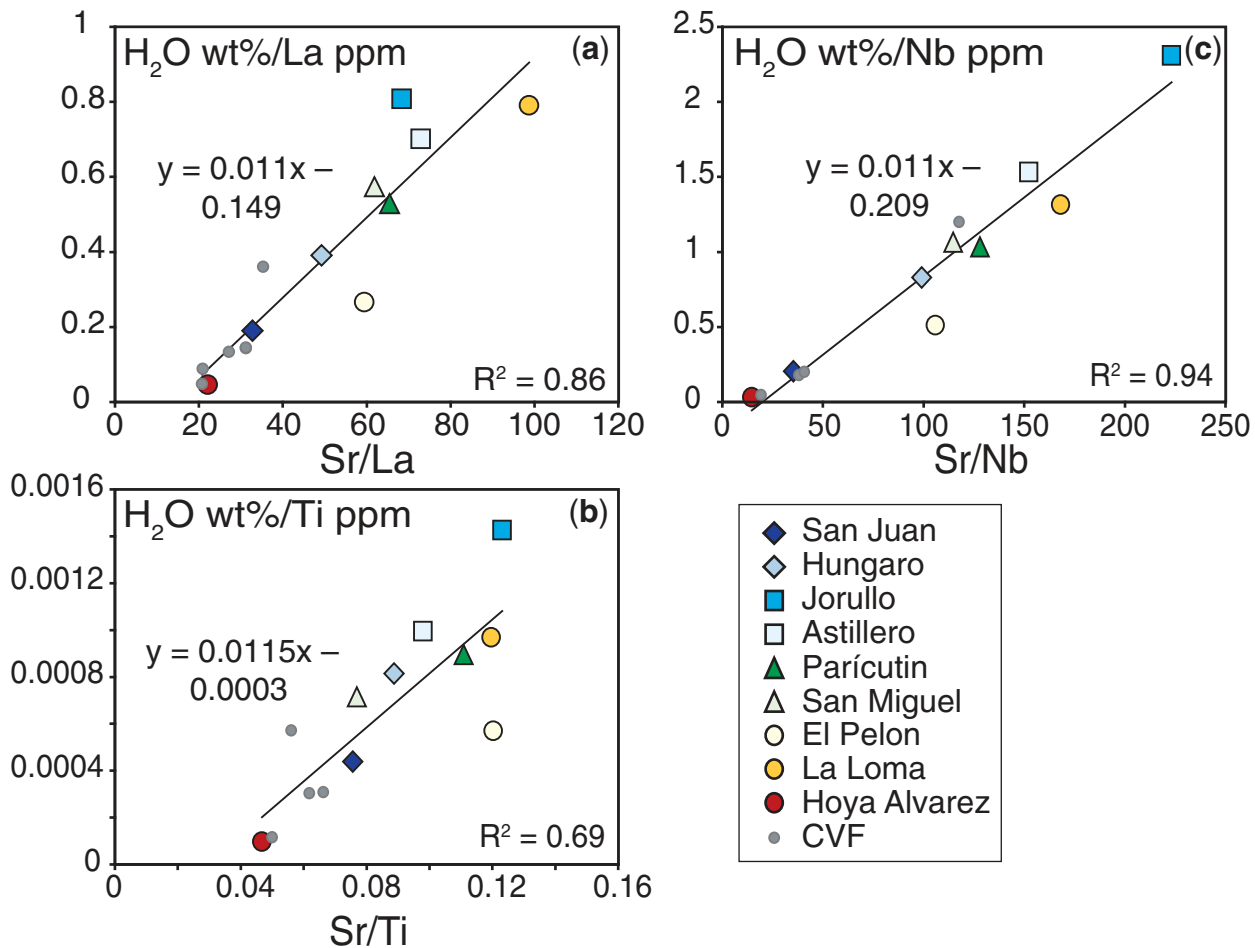
Fig. 10. Relationships between H_2O and trace element ratios for MGVF and CVF Chichináutzin melt inclusions. CVF data are from Cervantes & Wallace (2003). Linear fits to the data were used to calculate H_2O contents for magmas throughout the MGVF and other regions of central Mexico using previously published whole-rock trace element data (see Fig. 11).

but the volcanic front magmas generally contain high H_2O contents. In addition to the error assessment described above for the H_2O estimates, the calculated H_2O contents of the ZVB magmas and the inferred pattern of decreasing H_2O with distance from the trench both agree with the H_2O estimates of Blatter *et al.* (2007) based on experimental phase equilibria.

MANTLE HETEROGENEITY BENEATH THE MGVF

The variations in Nb and Ta in the MGVF primary melts (Fig. 6) and elsewhere in the TMVB are large enough that they cannot be explained solely by variations in the degree of partial melting of a single mantle source, which suggests that the mantle beneath the TMVB is heterogeneous in composition (Luhr, 1997; Wallace & Carmichael, 1999; Cervantes & Wallace, 2003; Straub *et al.*, 2008).

This heterogeneity may be related to a slab window that passed beneath the region to the north of the Pliocene–Quaternary volcanic arc from ~11·5 to 6 Ma, which allowed sub-slab mantle to flow upwards into the slab gap (Ferrari, 2004). Alternatively, it may be related to advection of OIB-type mantle from behind the arc as a result of corner flow in the mantle wedge (Luhr, 1997).

The composition of the mantle wedge can be inferred from HFSE (Nb, Ta, Ti, Zr), heavy rare earth elements (HREE), and Y abundances in arc magmas because these elements have relatively low solubilities in fluids under most conditions relevant to slab dehydration (Pearce & Peate, 1995; Kessel *et al.*, 2005). However, Kessel *et al.* (2005) found that Nb and Ta can become mobile at temperatures $\geq 900°C$ as a result of rutile breakdown in subducted metabasalt, such that these elements may not behave conservatively in the wedge. This issue will be revisited below, but we emphasize here that our
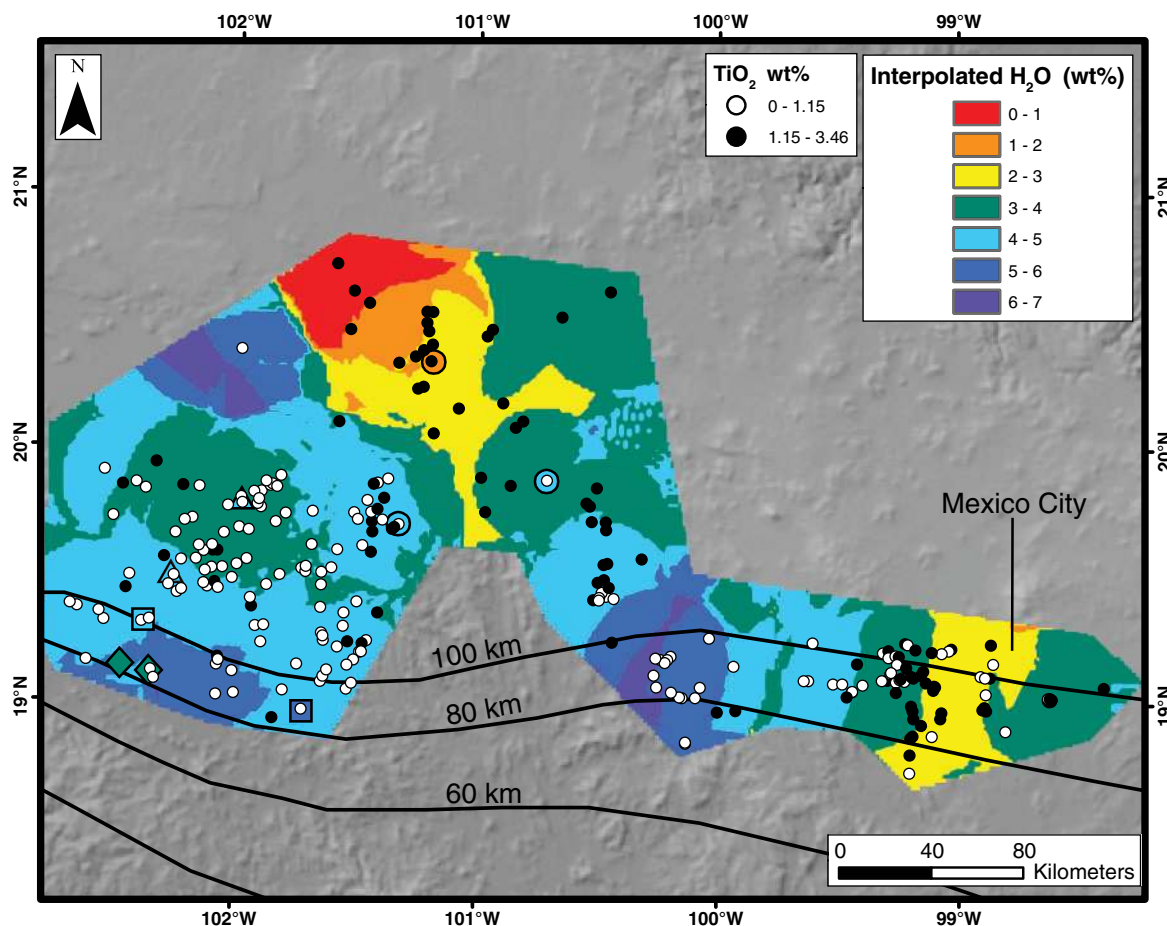
Fig. 11. Map of calculated H_2O contents across central Mexico. The small open and filled circles represent the locations of cones for which H_2O contents were calculated using the correlations shown in Fig. 10 together with published whole-rock trace element data (Hasenaka & Carmichael, 1985; Blatter *et al.*, 2001; Cervantes & Wallace, 2003; Siebe *et al.*, 2004; Schaaf *et al.*, 2005; Gomez-Tueña *et al.*, 2007). The map was produced using the kriging function in ArcMap, where H_2O contents were interpolated over a defined space, and the H_2O concentrations were then contoured, grading from warm colors (low H_2O) to cool colors (high H_2O). Also shown (larger symbols) are the locations of the MGVF samples from this study (data points are color coded by H_2O content using the same colors as shown in the legend) and contours to the top of the subducting slab (Pardo & Suárez, 1995). Some small-scale features in the interpolated values (e.g. along the NW side) are artefacts of the kriging procedure. The TiO_2 concentrations of samples for which we have calculated H_2O are also indicated (open circles, <1·15 wt % TiO_2; filled circles, >1·15 wt % TiO_2). There is a strong spatial relationship between regions of low melt H_2O and high TiO_2.

interpretations are based on a combination of data for HFSE, HREE, and Y. Concentrations of Nb and Y in the primary melts suggest that most MGVF magmas originated from mantle that is less depleted, to varying degrees, than the depleted MORB mantle (DMM) source (Fig. 13). The magmas range from OIB-like (Hoya Alvarez) to depleted compositions (Jorullo) that are close to melts derived from DMM sources. In contrast, mantle sources for Kamchatkan basalts tend to be more depleted, similar to DMM (Portnyagin *et al.*, 2007). In both Mexico and Kamchatka, variations in the HFSE, HREE, and Y contents of the magmas are consistent with the interpretation that the mantle wedge has been variably depleted by partial melting and melt extraction before it is overprinted by an H_2O-rich component from the slab that triggers flux

melting (Luhr, 1997; Wallace & Carmichael, 1999; Cervantes & Wallace, 2003; Portnyagin *et al.*, 2007; Straub *et al.*, 2008). Whether the OIB mantle component beneath Mexico was introduced through a slab window or by advection of asthenospheric mantle from behind the arc, it has been variably depleted by previous partial melting to create a spectrum of mantle compositions beneath the TMVB.

Primary melt compositions are spatially heterogeneous, both along and across the arc. For example, melts along the volcanic front show variations in both the extent of Nb and Ta depletion and the influence of subduction-related components over short spatial distances. Jorullo and Astillero (∼80 km apart) melts have low Nb and Ta concentrations and high concentrations of fluid-mobile
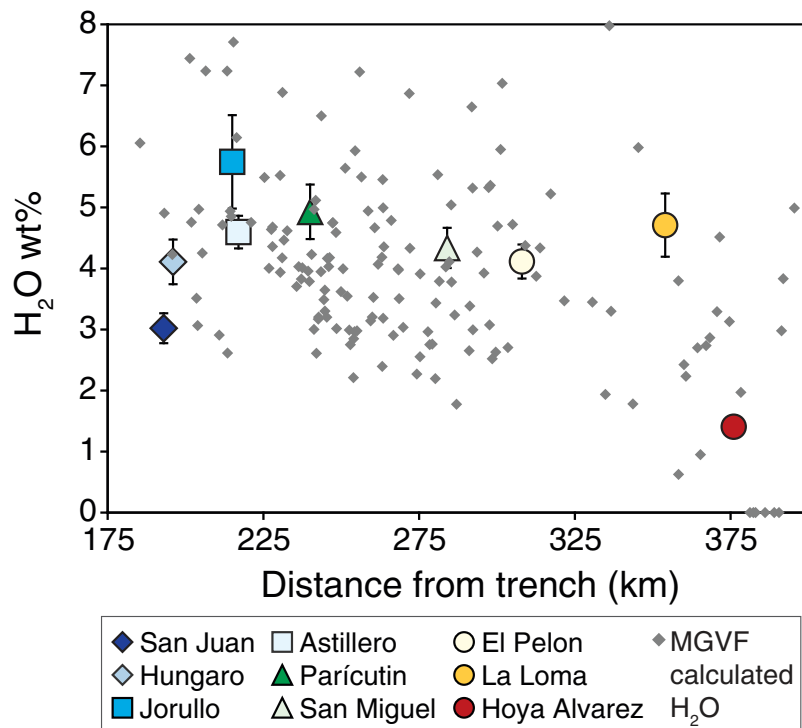
Fig. 12. Melt H_2O contents vs distance from the trench for all MGVF localities. The small grey diamonds are the localities in the MGVF where H_2O contents were calculated using the correlations shown in Fig. 10. Uncertainties on calculated H_2O values are $\pm 1\cdot 4$ wt % H_2O. Also shown are the maximum melt inclusion H_2O concentrations measured in this study (Table 1). Cones with high (>7 wt %) calculated H_2O concentrations typically have ratios of H_2O to incompatible trace elements that are higher than those for any of our samples used in the calibration, making these high calculated values subject to larger uncertainty.
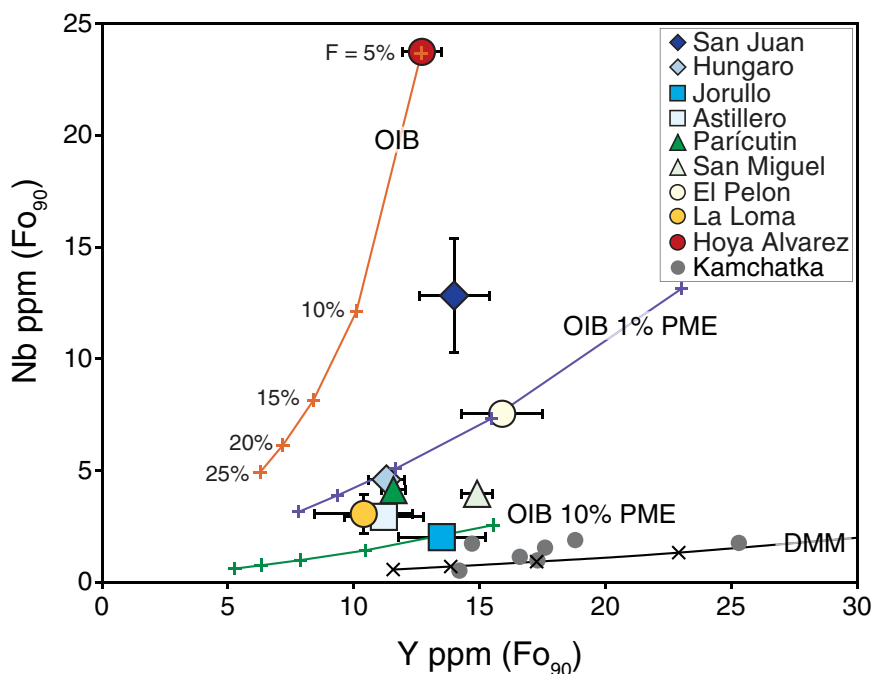
Fig. 13. Primary melt Nb vs Y for the MGVF (Table 4) and Kamchatka (Portnyagin *et al.*, 2007). Lines show variable batch partial melts of four mantle source compositions. The OIB source is calculated as described in the text by assuming that the Hoya Alvarez primary melt represents a 5% partial melt of garnet lherzolite. The DMM source is from Workman & Hart (2005). Lines for OIB 1% PME and OIB 10% PME represent melting of an initially OIB source that has been depleted by 1% and 10% previous melt extraction, respectively, as described in the text.

elements such as Ba and Pb (Fig. 6). However, the other arc-front volcanoes have much more variable primary melt compositions. Hungaro is less depleted in Nb and Ta than Jorullo and Astillero, and San Juan, located only 12 km from Hungaro, lacks the depletion entirely (Fig. 6). Primary melts from far behind the volcanic front exhibit similar trench-parallel spatial variability. La Loma shows large Nb–Ta depletions whereas Hoya Alvarez (70 km away) has high Nb and Ta (Fig. 6). Additionally, Hoya Alvarez lacks the subduction signature seen at the other volcanoes, with the lowest Ba/La and Pb. Together these data suggest that the mantle beneath Hoya Alvarez is less depleted and has not been significantly influenced by fluids or hydrous melts from the subducting slab.

The heterogeneities in melt compositions correspond to variations in H_2O content in the TMVB. There are two notable transitions from H_2O-rich magmas to more H_2O-poor magmas; one in the northeastern part of the MGVF and the other in the CVF (Fig. 11). In the northeastern part of the MGVF, magmas have a range of H_2O contents, but a number of volcanic centers (mostly maar and tuff ring eruptions of alkali basalt similar to Hoya Alvarez) have ≤2 wt % H_2O, values that are lower than those elsewhere in the MGVF (Fig. 12). The trace element compositions of low-H_2O magmas in the NE MGVF and in the CVF appear to be distinct as well. Because HFSE concentrations are indicative of the mantle source region (Figs 5 and 6), we plotted TiO_2 concentrations on the map of H_2O (Fig. 11). The magmas in the low-H_2O regions generally have higher TiO_2 than do magmas in the high-H_2O regions. The melt inclusion trace element data from Hoya Alvarez, located in the NE MGVF, suggest that the mantle source for this volcano is OIB-like, with high Nb and Ta. Thus, we conclude that the low-H_2O magmas are generally derived from OIB-type mantle source regions.

MODELING PARTIAL MELTING AND SUBDUCTION-RELATED ENRICHMENT OF THE MANTLE WEDGE

The primary melt compositions determined from the melt inclusion data allow us to estimate: (1) degrees of mantle melting (F) across the arc; (2) mantle volatile concentrations; (3) compositions of mantle sources before subduction-related enrichment; (4) compositions of H_2O-rich slab-derived components. These parameters were calculated using the inverse modeling approach described by Portnyagin et al. (2007) and modified as described below. This method assumes modal batch melting as an approximation to pooling of melts formed by polybaric, near fractional melting, based on the rationale presented by Kelley et al. (2006).

The first step in the modeling is to establish the mantle source compositions before addition of subduction-derived components. As discussed above, heterogeneous mantle sources in the MGVF and TMVB appear to involve previous melt extraction (PME) by small degrees of melting that leave the wedge variably depleted in HFSE, HREE and Y. Because the intraplate alkali basalt magmas like those of Hoya Alvarez are derived from mantle sources that have not been affected by previous melt extraction, we assume that their mantle sources best approximate the composition of the wedge before depletion, and that formation and extraction of such magmas causes the depletion event. We therefore assumed that the Hoya Alvarez primitive melt formed from this undepleted mantle source by 5% partial melting (see Eiler et al., 2005) and that melting occurred in the garnet peridotite stability field because of the high Dy/Yb of this composition (Fig. 5). This evidence for an initially OIB-type mantle source contrasts with data for Kamchatka (Fig. 13), where enriched DMM (Workman & Hart, 2005) was the most enriched mantle required and PME occurs in the spinel peridotite stability field (Portnyagin et al., 2007).

For each primitive melt composition, we determined best-fit amounts of PME (from the initial OIB mantle source) and F (from the mantle after PME) by minimizing the residual error of F estimated from five incompatible trace elements (Nb, Ti, Dy, Yb, Y; see Portnyagin et al., 2007, for complete details). Although high slab temperatures might cause Nb to become mobile (at $T \geq 900°C$; Kessel et al., 2005), and thus invalidate its use in this calculation, which is predicated on conservative element behavior in the mantle wedge, we obtain similar results for amounts of PME and F values if Nb is left out of the calculation.

The relatively high Dy/Yb (greater than the MORB value of 1·5) of the MGVF primitive melts (Fig. 6h) suggests that garnet may have been present in the mantle source region during melting. To test this, we modeled melting of both garnet and spinel peridotite. For all primitive melts the residuals are much smaller when PME occurs in the garnet stability field, followed by flux-melting in the spinel field. These models produce primitive melt compositions with Dy and Yb abundances similar to the observed values. Because melting of a garnet-bearing source during PME causes a slight decrease in the Dy/Yb of the mantle residuum, the residuum can later be flux-melted in the spinel field to yield magmas that have Dy/Yb values that are intermediate between typical OIB and MORB values (Fig. 6h). The presence of garnet in the source region for the OIB-type magmas in the MGVF is at odds with results from the western TMVB. Luhr (1997) suggested that OIB and calc-alkaline melts in western Mexico originated from different source regions, with OIB melts tapping spinel lherzolites (shallower melting)

Table 5: Compositions of H_2O-rich subduction components and parameters of mantle melting

	San Juan	Hungaro	Jorullo	Astillero	Parícutin	San Miguel	El Pelon	La Loma	Hoya Alvarez*
Rb	202	114	59	62	81	73	209	106	
Ba	4832	3375	1479	2024	2297	2105	3800	1697	
U	2·8	3·1	1·0	1·6	2·4	1·9	6·4	3·6	
Th	8·9	5·1	3·1	4·1	6·0	5·9	14·6	9·8	
K_2O (wt %)	7·5	9·1	5·7	6·9	7·8	6·3	9·5	8·8	
Cl	12577	12568	11213	13760	9880	11174	11826	13305	
La	95	98	50	60	65	68	134	49	
Pb	68	54	33	33	44	34	59	35	
H_2O (wt %)	48	51	54	48	51	49	49	62	
Ce	342	215	109	145	160	190	337	116	
Sr	6265	5422	4060	5054	5516	5117	9214	6006	
Nd	193	95	74	84	75	81	146	61	
Zr	809	683	550	369	427	565	957	349	
Sm	35	14	14	20	21	33	23	12	
Na_2O (wt %)	43	38	39	43	40	43	39	28	
$\sum$ residuals	0·22	0·26	0·28	0·17	0·2	0·21	0·17	0·3	
PME	0	0·015	0·105	0·031	0·016	0·031	0·01	0·023	0
F	0·112	0·124	0·065	0·127	0·135	0·091	0·088	0·147	0·05
Error *F*	0·013	0·01	0·009	0·01	0·012	0·009	0·007	0·019	
Wt % SC added	0·53	0·98	0·8	1·06	1·24	0·75	0·67	1·14	0
Mantle H_2O (wt %)	0·3	0·51	0·44	0·53	0·66	0·38	0·35	0·72	0·04
Mantle Cl (ppm)	82	125	91	148	125	85	83	153	14

All concentrations are in ppm, except for K_2O, H_2O, and Na_2O, which are in wt %. $\sum$ residuals is the sum of residuals for Nb, Ti, Dy, Y and Yb between the actual composition of the primitive melt (Table 4) and the model melt formed by melting of the subduction modified source. PME is the weight fraction of previous melt extraction during an earlier melting and depletion event in the source. *F* is the weight fraction of partial melting to generate the primitive melts in Table 4. Wt % SC added is the amount of H_2O-rich subduction component added to the source after PME. Mantle H_2O and Cl are the concentration of H_2O (in wt %) and Cl (in ppm) in the mantle source after enrichment by the subduction component. Compositions of mantle sources after PME and after addition of the SC are given in Electronic Appendix 4.
*Mantle source composition for Hoya Alvarez was calculated by assuming that the primitive melt (Table 4) formed by 5% partial melting of garnet lherzolite.

and calc-alkaline melts generated from garnet lherzolite (deeper melting). These conclusions were based on higher Yb and lower Dy/Yb in the alkaline magmas compared with calc-alkaline samples. However, the MGVF magmas illustrate the opposite, with higher Dy/Yb in the Hoya Alvarez alkaline magma.

Results of the model calculations are given in Table 5, and values for all partition coefficients used are given in Table 6 (mantle compositions are reported in Electronic Appendix 4). Based on these model calculations, the primitive melts in the MGVF (excluding Hoya Alvarez, for which *F* was assumed to be 5%) form by 6–15% partial melting of mantle sources that had mostly experienced 0–3% PME, although the source for one cone (Jorullo) required 10% PME. The calculated *F* values for the MGVF primitive magmas are identical to those calculated for Kamchatka using similar methods (5–14%; Portnyagin *et al.*, 2007), despite the large differences between the two arcs in mantle source compositions both before and after PME. As emphasized by Portnyagin *et al.* (2007), these *F* values are dependent on the assumed initial mantle source composition (before PME) and the partition coefficients that are used, and variation of the initial source in the Kamchatka case can change estimated extents of melting by ∼3% (absolute). We found that other choices of initial source composition resulted in substantially poorer fits (larger sum of residuals). The presence of samples like Hoya Alvarez in the MGVF that are plausible melts formed by the PME process improves our ability to constrain the initial mantle wedge composition

Table 6: Mineral–melt distribution coefficients

	Olivine	Opx	Cpx	Spinel	Garnet
Rb*	0·00001	0·0001	0·002	0·002	
Ba	0·0003	0·0001	0·00068	0·0005	
U	0·00002	0·0002	0·0038	0·01	
Th	0·00005	0·0001	0·013	0·01	0·0006
K	0·00005	0·0001	0·0072	0·001	0·05
Nb	0·00004	0·002	0·0077	0·4	
La	0·00003	0·00005	0·054	0·003	
Pb	0·008	0·008	0·008	0·008	
Ce	0·0001	0·0002	0·09	0·003	0·01
Sr	0·0015	0·0005	0·13	0·1	0·006
Nd	0·0004	0·0005	0·15	0·005	0·071
Zr	0·0007	0·014	0·123	0·4	0·47
Sm	0·001	0·0015	0·25	0·0075	0·34
Na	0·001	0·0015	0·25	0·0075	
Ti	0·032	0·215	0·358	0·167	0·28
Dy	0·001	0·008	0·4	0·008	3·2
Y†	0·01	0·01	0·4	0·023	4·1
Yb‡	0·024	0·038	0·22	0·007	7·4

Except where noted, all partition coefficients for olivine, opx, cpx and spinel are from Eiler *et al.* (2005), and those for garnet are from Gaetani *et al.* (2003). Bulk *D* values were used for H_2O (0·012, Kelley *et al.*, 2006) and Cl (0·003, Portnyagin *et al.*, 2007).
*All values for Rb are from Eiler *et al.* (2000).
†Values for Y in olivine, opx, cpx and spinel are from Eiler *et al.* (2000).
‡Values for Yb in olivine, opx and cpx are from Grove *et al.* (2002).

(before PME and subduction-related enrichment) beneath this region.

The final step in the melting model is to use the value of *F* together with the concentrations of all volatiles and incompatible elements in each primitive melt composition to calculate a mantle source composition after subduction-related enrichment for each cone (Portnyagin *et al.*, 2007). The results of these calculations indicate that the subduction-modified source for each cone (except Hoya Alvarez) has higher concentrations of all incompatible elements and volatiles [except those used to calculate *F* values (Nb, Ti, Dy, Yb, Y), which were assumed to be derived only from the mantle wedge] than the mantle sources calculated after PME. These differences reflect the addition of a hydrous component from the slab to the mantle wedge. The composition of this hydrous component was calculated by assuming that the sum of all incompatible elements as oxides plus H_2O and Cl equals 100% (Stolper & Newman, 1994; Cervantes & Wallace, 2003; Eiler *et al.*, 2005; Portnyagin *et al.*, 2007).

MANTLE VOLATILE CONCENTRATIONS, TEMPERATURES, AND PARTIAL MELTING PROCESSES

Calculated mantle H_2O concentrations are high beneath most of the MGVF (0·3–0·7 wt % H_2O), with lower values at Hoya Alvarez (0·04 wt %) (Table 5). Mantle Cl contents range from 80 to 150 ppm but are also lower for Hoya Alvarez (14 ppm) (Table 5). The mantle H_2O concentrations, with the exception of those for Hoya Alvarez, are higher than most values for the mantle wedge beneath the Kamchatka arc (0·13–0·4 wt %; Portnyagin *et al.*, 2007) and back-arc basins (≤0·38 wt %; Kelley *et al.*, 2006) and are significantly higher than DMM (70–450 ppm; Sobolev & Chaussidon, 1996; Workman & Hart, 2005) and OIB sources (<900 ppm; Dixon *et al.*, 1997; Wallace, 1998). Similarly, the MGVF mantle Cl concentrations are higher than primitive mantle (0·4–17 ppm; McDonough & Sun, 1995). As with the primary melt volatile concentrations, there is no trend in across-arc mantle H_2O or Cl, and the persistence of high mantle volatile contents across a broad region requires influence of subduction-related H_2O-rich component(s) beneath a large portion of the arc. Our results for the MGVF are in contrast to those for Kamchatka, where there is an apparent decrease in the H_2O concentrations of the mantle wedge with increasing distance from the trench (Portnyagin *et al.*, 2007).

Given that the depth to the subducted slab beneath the volcanic front of the MGVF is about 80–100 km, many of the estimated mantle H_2O concentrations for the MGVF are greater than the maximum amount that can be stored in nominally anhydrous minerals (~0·3 wt % at 100 km increasing to ~0·45 wt % at 150 km; Hirschmann *et al.*, 2005). This requires that H_2O in the mantle source is partly contained in hydrous minerals or in a fluid or hydrous melt phase (or both). Rare hornblende-bearing ultramafic xenoliths occur in the ZVB volcanic field to the east of the MGVF, but the xenoliths have compositions that are inconsistent with them representing either the source of the lavas in that region or mantle residuum after melting (Mukasa *et al.*, 2007). Olivine–hornblende trachybasalts with higher K_2O than the calc-alkaline magmas in this study occur in the MGVF but are uncommon (Luhr & Carmichael, 1985; Hasenaka & Carmichael, 1987), and they could potentially be an indicator of the presence of hornblende-bearing mantle sources. Although factors such as temperature and melt composition affect hornblende stability in mafic magmas, we interpret the absence of hornblende phenocrysts in most mafic magmas from the MGVF to be an indication that this phase is not the main repository of the extra H_2O in the mantle source. Instead, we suggest that the high inferred mantle
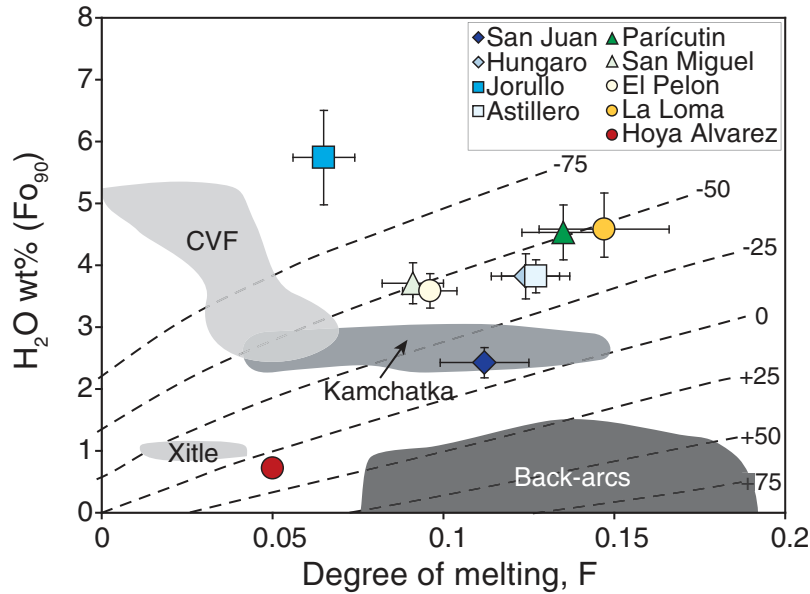
Fig. 14. Primary melt H_2O (Table 4) and the calculated degree of partial melting of the mantle (F) in weight fraction melt (Table 5). Dashed curves represent temperature deviations (°C) from the dry peridotite solidus (Portnyagin *et al.*, 2007). The position of the MGVF data below the dry peridotite solidus temperature indicates a strong role for fluxing by H_2O-rich fluids or melts in the formation of primitive melts in this region. Other regions shown for comparison are the Chichináutzin Volcanic Field (CVF) [light gray fields show data for Xitle volcano (lower field) and other cinder cones (upper field); Cervantes & Wallace, 2003; F values for the CVF cones were calculated using the same procedures as for the MGVF primitive melts], the Kamchatka Arc (medium gray field; Portnyagin *et al.*, 2007) and back-arc basins (dark gray field; Kelley *et al.*, 2006). The values of weight per cent H_2O for Kamchatka are the maximum measured values in melt inclusions, to be consistent with the approach used here for MGVF melt inclusions.

source H_2O values for the MGVF are the result of fluids or hydrous melts from the subducted slab. Because of the strong effect of H_2O in lowering melting temperatures, the relationship between primitive melt H_2O content (which is related to mantle source H_2O content) and melt fraction can be used to estimate mantle temperatures (Fig. 14). Using this relationship, data on primitive MGVF melt compositions can provide information on the mantle wedge thermal structure. Most of the MGVF primitive melt compositions indicate mantle temperatures that are 40–50°C lower than the melting temperature of dry peridotite (Fig. 14), and therefore temperatures of 1225–1290°C can be inferred for the mantle wedge beneath the MGVF at 1·5–2 GPa [based on dry peridotite solidus from Katz *et al.* (2003)]. This is a clear indication that melting is driven by the introduction of a slab-derived H_2O-rich component, because relatively high mantle H_2O is required to create F values of 9–15% at such low temperatures. The temperature inferred for the Jorullo source region is significantly lower (∼100°C below the dry peridotite solidus), and that inferred for San Juan, also located along the volcanic front, is significantly higher (∼10°C below the dry peridotite solidus). Interestingly, the source region for Jorullo is also interpreted to have been the most depleted by PME whereas the source for San Juan is the least depleted (Fig. 13); in many regards, the source region

for San Juan is similar to that for Hoya Alvarez but has been overprinted by a subduction-related H_2O-rich component.

Hoya Alvarez, which is the farthest locality from the trench, originated from a much less depleted (OIB-type) source region and has low concentrations of fluid-mobile elements, H_2O and Cl, suggesting that the mantle had not experienced previous melt extraction or significant hydration by subduction processes. Although the extent of melting (5%) for Hoya Alvarez shown in Fig. 14 was an assumed value used in our melting model, the low H_2O of the Hoya Alvarez magma indicates that for a wide range of potential F values, melting would have occurred at or above the dry peridotite solidus. In this regard the Hoya Alvarez composition is similar to other back-arc basin magmas (Fig. 14). Such low-H_2O melts in subduction zones form primarily by decompression melting (Sisson & Layne, 1993; Sisson & Bronto, 1998), probably because there is a component of upwelling associated with the corner-flow-driven advection of mantle from behind the arc (Tatsumi & Eggins, 1995; Luhr, 1997; Grove *et al.*, 2002). Our data suggest that low-H_2O, transitional to alkalic magmas erupted at Hoya Alvarez and other localities far behind the front (Fig. 11) result from decompression melting of the mantle, with little to no involvement of slab-derived fluids. One volcano (Xitle) from the CVF
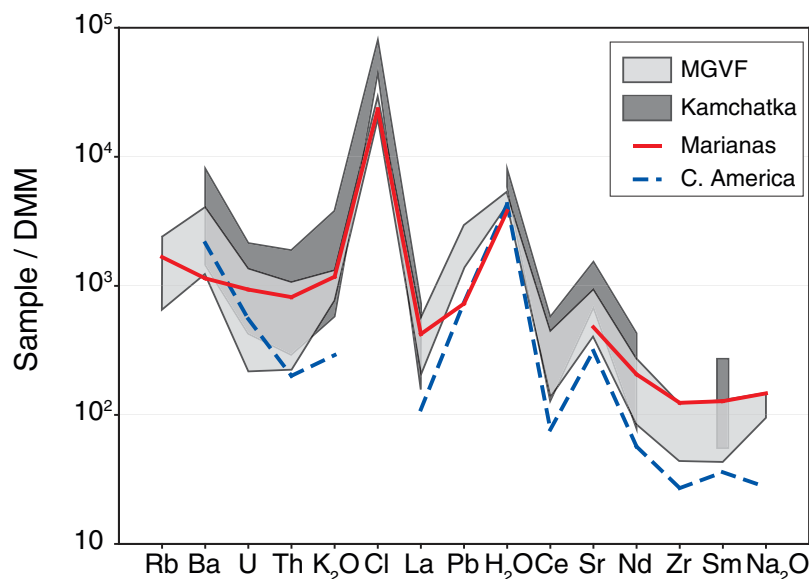
Fig. 15. Selected abundances of trace elements, H_2O and Cl in calculated H_2O-rich subduction components for the MGVF (Table 5). Shown for comparison are subduction components calculated for Kamchatka (dark gray field; Portnyagin *et al.*, 2007), Marianas (continuous line; Stolper & Newman, 1994), and Central America (dashed line; Eiler *et al.*, 2005). All concentrations are normalized to DMM (Salters & Stracke, 2004).

also erupted magma with low H_2O and similar chemical characteristics to Hoya Alvarez; this magma is also interpreted to have formed primarily by decompression melting (Cervantes & Wallace, 2003).

In contrast to results from the MGVF, H_2O-rich primitive calc-alkaline magmas from the CVF region appear to have formed by low degrees of melting ($\leq 10\%$; see Fig. 14; see also Wallace & Carmichael, 1999; Portnyagin *et al.*, 2007). Crustal thickness beneath the CVF ($\sim 45-50$ km) is the greatest of any region in the TMVB, whereas the crustal thickness beneath the MGVF is ~ 35 km (Wallace & Carmichael, 1999, and references therein). The contrasts in degree of melting for H_2O-rich magmas in the MGVF and CVF suggest that the thickness of the crust or lithosphere limits the maximum extent of flux melting in arcs, perhaps by limiting the thickness of convecting asthenospheric mantle caused by corner flow and thus limiting the maximum temperature that can be attained in the wedge (Fig. 14).

ORIGIN OF H_2O-RICH SUBDUCTION COMPONENTS

The H_2O-rich components added to the mantle wedge beneath the MGVF (Fig. 15) are similar in composition to those calculated for the Marianas (Stolper & Newman, 1994), Central America (Eiler *et al.*, 2005), and Kamchatka (Portnyagin *et al.*, 2007). The amounts of fluid added to the mantle wedge (0·5–1·2 wt %) are also generally similar to estimates for these other arcs (0–0·5 wt %

for Marianas; 0·3–4 wt % for Central America; 0·15–0·42 wt % for Kamchatka). These similarities are notable given the large differences in subducted plate age and the thickness and composition of subducted sediment in these arcs.

The high magmatic volatile concentrations for large distances across the MGVF are puzzling. In 'warm-slab' subduction zones such as Mexico devolatilization of hydrous phases in the downgoing slab should occur mainly beneath the forearc because of the thermal state of young oceanic lithosphere when it is subducted (Kerrick & Connolly, 2001; Schmidt & Poli, 2004; Rondenay *et al.*, 2008). In the following sections, we use a combination of trace element data, estimated compositions of H_2O-rich components, $\delta^{18}O_{olivine}$ values, and 2-D geodynamic models of the subducted slab and mantle wedge to test hypotheses regarding the origin of subduction-related H_2O-rich components beneath the MGVF.

Trace element evidence for sediment involvement

To distinguish between potential sources for the H_2O-rich components added to the mantle wedge beneath the MGVF, we compared the trace element composition of the H_2O-rich components determined from the melt inclusion data with hypothetical compositions of both fluids and melts derived from subducted oceanic crust and sediment (Fig. 16). For these calculations, we used bulk compositions of sediments on the Cocos Plate (Lagatta, 2003), an average altered oceanic crust
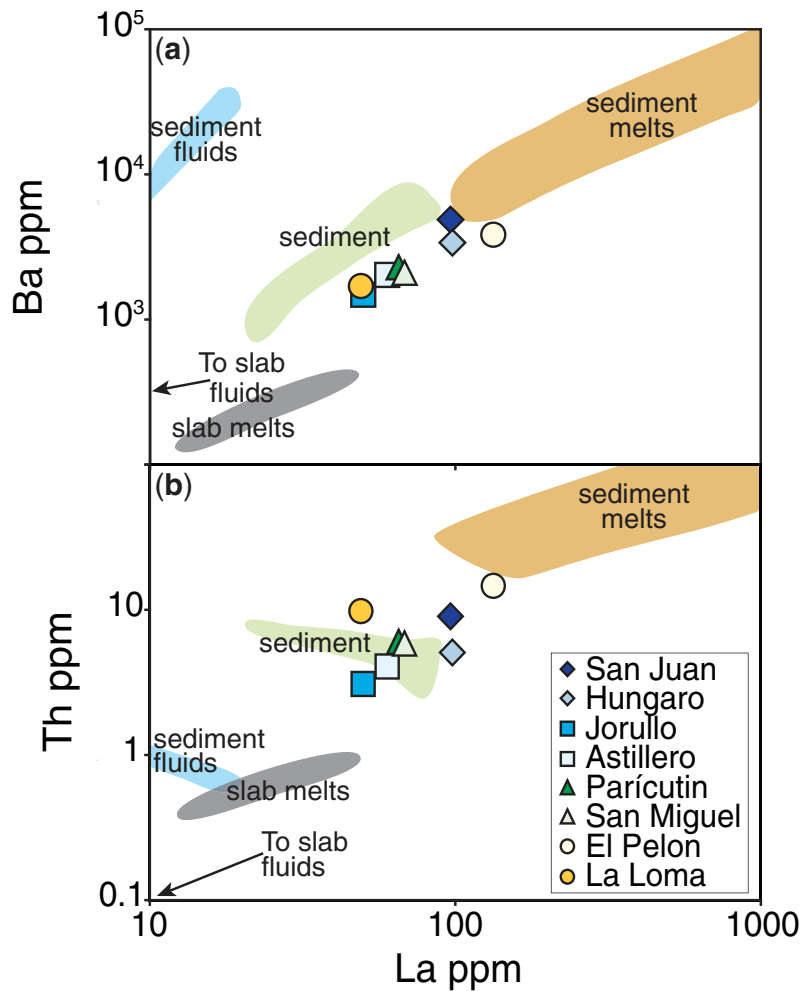
Fig. 16. Concentrations of Ba (a) and Th (b) vs La in the H_2O-rich subduction components for the MGVF. Shown for comparison are the compositions of hypothetical fluids and partial melts from oceanic crust calculated using an average oceanic crust composition (Staudigel *et al.*, 1995), and fluids and partial melts of subducted sediment calculated from Cocos plate sediment data (shown by light shaded fields) from Lagatta (2003). All fluids were calculated using fluid–solid *D* values at 4 GPa and 700°C from Kessel *et al.* (2005), and melts were calculated using fluid–solid *D* values at 4 GPa and 1000°C from Kessel *et al.* (2005).

composition (Staudigel *et al.*, 1995), and fluid–eclogite and melt–eclogite *D* values (Kessel *et al.*, 2005), which are appropriate for both metabasalt and pelitic and siliciclastic metasediments. Comparison of Ba, Th, and La concentrations in the calculated H_2O-rich components and their hypothetical sources indicates that the subduction-recycled material added to the MGVF mantle wedge is a combination of oceanic crust and sediment components (Fig. 16). Some of the modeled H_2O-rich components plot near the slab fluid field, suggesting less involvement of sediments, whereas other H_2O-rich components have higher Ba, Th, and La concentrations, suggesting greater proportions of sediment melt.

Although the sediment package subducted at the Middle America Trench is relatively thin (~170 m; Plank & Langmuir, 1998; Lagatta, 2003; Manea *et al.*, 2003) compared with many other subduction zones, the modeled

H_2O-rich component compositions for the MGVF show clear evidence for involvement of recycled sediment. Cocos Plate sediments have a range of Th/La values (Lagatta, 2003); higher values are found in the upper part of the section (~100 m of continentally derived hemipelagic sediment) and lower values in the lower part of the section (hydrothermally altered pelagic sediment). Importantly, the relatively high La and Th of the calculated H_2O-rich components (Fig. 16) requires partial melts of subducted sediment rather than fluids derived by metasediment dehydration at temperatures <~700°C (Kessel *et al.*, 2005; Plank, 2005, and references therein). The relatively high K_2O/H_2O of MGVF primary melts is also consistent with data for sediment melts (Hermann & Spandler, 2008). Although the trace element data do not allow us to discriminate whether the oceanic crustal component is a fluid or a hydrous melt, the geodynamic

models discussed below suggest that temperatures in the subducted oceanic crust are at least 200–300°C too low to produce partial melting (based on Kessel *et al.*, 2005), and thus fluids seem more likely. At the pressures involved (~2–4 GPa), there is a miscibility gap between hydrous melts and fluids, so the H_2O-rich component will not be a supercritical liquid with melt-like solubilities of trace elements (Kessel *et al.*, 2005). Our conclusion that the basaltic slab beneath the MGVF does not melt contrasts with the trace element and isotopic evidence cited in favor of slab melting beneath the ZVB region to the east (Gomez-Tueña *et al.*, 2007).

Mixing of an oceanic crust component and sediment melts is also evident in plots of Ce and Pb vs La, but the relationship fails for Rb, Sr and Zr (not shown). For Rb, the H_2O-rich components calculated for MGVF primitive melts have lower Rb than mixtures of oceanic crust and sediment components. The opposite is observed for Sr and Zr, which have higher concentrations in the H_2O-rich components than can be produced by either slab or sediment fluids or melts. However, as seen in Fig. 15, the subduction components calculated for the MGVF (including Sr and Zr) are very similar to those calculated for other arcs worldwide. Calculated subduction components generally contain high levels of Sr (3000–15 000 ppm; Stolper & Newman, 1994; Eiler *et al.*, 2000; Portnyagin *et al.*, 2007), but dehydration or melting of oceanic crust or sediment cannot produce such high concentrations. One possibility is that the presence of components such as Cl, F, and S in subduction-derived fluids changes the partitioning of elements compared with experimental systems lacking these elements. Another possibility is that mineral breakdown reactions in natural systems are more complex than in equilibrium experiments, leading to greater concentrations of some elements in the fluid phase (e.g. John *et al.*, 2008).

Oxygen isotope constraints

Because oxygen is a major element in silicate melts, the high $\delta^{18}O_{olivine}$ values found in the MGVF magmas provide an important mass-balance constraint on the origin and amounts of H_2O-rich subduction components that must be added to the mantle wedge. Fluids or hydrous melts derived from subducted sediment and altered oceanic crust should have higher $\delta^{18}O$ than normal mantle values. The uppermost altered oceanic crust has $\delta^{18}O$ values of 7–15‰ (Alt *et al.*, 1986; Staudigel *et al.*, 1995), and hemipelagic and pelagic sediments are even more isotopically heavy (15–25‰; Kolodny & Epstein, 1976; Arthur *et al.*, 1983; Alt & Shanks, 2006). Fractional crystallization of primitive magma can increase $\delta^{18}O$ values by ≤0·1–0·3‰ (e.g. Bindeman *et al.*, 2004), but the MGVF magmas are compositionally primitive, with evidence for only minor fractionation of olivine. Although crustal assimilation can also increase $\delta^{18}O$ values of arc magmas

(Harmon & Hoefs, 1995), the primitive nature of the MGVF melts suggests that this process is unlikely to have had an effect on a major element such as oxygen.

The high $\delta^{18}O$ values in olivines from the MGVF most probably originated from components with heavy $\delta^{18}O$ values such as altered oceanic crust and/or subducted sediment. Sediment melts, in particular, seem likely given the high $\delta^{18}O$ values of subducted sediment and our interpretations based on trace element systematics. For example, volcanic rocks with $\delta^{18}O$ as high as +8‰ from Setouchi, Japan, have been interpreted as sediment melts (with initial $\delta^{18}O$ values of +30‰) that substantially re-equilibrated with peridotite during ascent through the mantle wedge (Bindeman *et al.*, 2005). Using a range of assumed $\delta^{18}O$ values for sediment and oceanic crust (no values for oceanic crust or sediment offshore of the TMVB have been measured), we calculated the effect that slab- and sediment-derived components would have on $\delta^{18}O$ values of partial melts generated from a fluxed mantle wedge and compared the results with the data for the MGVF (Fig. 17). For this purpose, we assumed that the $\delta^{18}O_{olivine}$ value (5·5‰) for Hoya Alvarez, which formed by decompression melting of mantle that was little affected by subduction processes, was representative of the mantle wedge before subduction-related enrichment.

Six of the cones have $\delta^{18}O$ values that are consistent with a single-stage hydrous enrichment model involving sediment melt, provided the pelagic and hemipelagic sediments subducting with the Cocos plate have $\delta^{18}O$ values of 15–25‰ (Fig. 17). The other two cones (Jorullo, San Miguel) have lower $\delta^{18}O$ values that could be explained by a combination of sediment melt and oceanic-crust-derived fluid. Three cones lie at the upper limit of compositions that could be produced by sediment melt addition and require that the sediment have $\delta^{18}O$ of +25‰ (Fig. 17). If actual Cocos plate sediment values are not this high, then the mantle sources for these samples would require some pre-enrichment in $\delta^{18}O$. Such pre-enrichment has been proposed to explain high $\delta^{18}O$ values in Kamchatka (Auer *et al.*, 2009) and Mt. Shasta in the Cascades (Martin *et al.*, 2009) by trenchward migration of the arc into a region overlying older, $\delta^{18}O$-enriched forearc mantle. The MGVF $\delta^{18}O$ values, however, do not show any correlation with distance from the volcanic front (Fig. 5d), in contrast to what would be expected if migration into enriched forearc mantle were involved.

Our results for the MGVF agree with the interpretations of Eiler *et al.* (2005) for Central America, where $\delta^{18}O_{olivine}$ values up to 5·7‰ were measured. They also concluded that these high values (which are slightly lower than those in the MGVF) required involvement of sediment melts, and they were able to explain these values with a single-stage hydrous enrichment model.
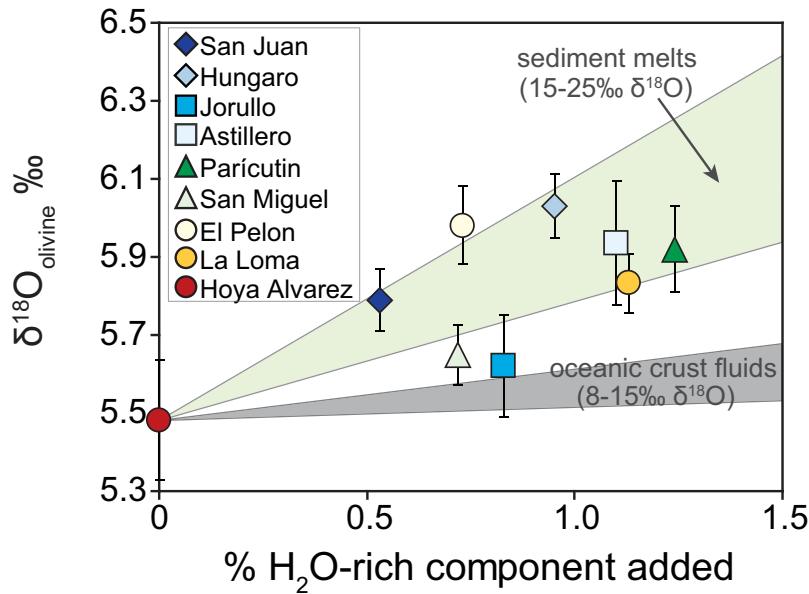
Fig. 17. Oxygen isotope ratios for MGVF olivines vs the calculated amounts of H_2O-rich subduction components added to the source region for each volcano. Shaded fields show the calculated effects of hydrous sediment melts and oceanic crust-derived fluids on partial melts formed by flux melting of the wedge. They are calculated by mass balance for bulk addition of the subduction component to the mantle wedge (e.g. Eiler *et al.*, 2005). For the calculations, we assumed that the hydrous fluids derived from the oceanic crust contained 50 wt % H_2O, similar to the values in the calculated subduction components (Table 5). For sediment melts, we assumed that 65% of the melt consisted of SiO_2, Al_2O_3, and other major elements that are not included in the calculated subduction components (Table 5). This results in 17·5 wt % H_2O in the sediment melts, and the elements in Table 5 (expressed as oxides) then account for the remaining 17·5 wt % of the melt. Because the sediment melt has a lower H_2O concentration than the fluid, forming a primitive melt with a given H_2O content requires a greater mass addition of sediment melt to the wedge compared with the amount of fluid that would be required. This causes the lower limit of the sediment melt field (for sediment melts with $\delta^{18}O$ of +15‰) to be at higher $\delta^{18}O$ values of the resultant magma than the upper limit of the oceanic crust-derived fluid field (for fluids with $\delta^{18}O$ of +15‰).

Dehydration of subducted components

Although trace elements and oxygen isotopes provide valuable information on the origin of H_2O-rich subduction components, understanding the thermal structure of the subduction zone is vital to assessing the depths at which fluids and hydrous melts will be released from the slab. Two-dimensional thermal models of the MGVF subduction zone were created to estimate the pressure–temperature (P–T) conditions of hydrous mineral breakdown reactions in the slab and melt generation in the mantle wedge. However, the history of subduction beneath the MGVF is complex, and therefore changes in subduction geometry over time must also be considered when assessing recycling of subducted components. Currently the subducting slab dips at an angle of $\sim$30° (Pardo & Suárez, 1995) beneath the MGVF, but there is evidence that the slab geometry has changed in the past 3 Myr. To the east of the MGVF, the Cocos slab trenchward of the Mexico City–Sierra Chichináutzin region is currently flat, and the space–time evolution of the TMVB shows that in the last 7 Myr the volcanic arc in the Mexico City region migrated $\sim$70 km toward the trench (Ferrari *et al.*, 1999). The change in position of the volcanic arc was caused by an increase in slab dip (Manea *et al.*, 2006). In the MGVF, there has been progressive trenchward movement of volcanism in the last 2 Myr, and between 3 Ma and the present, the Cocos plate geometry has probably steepened (Hasenaka & Carmichael, 1985; Ban *et al*, 1992). Based on this and the current differences in slab configuration between the MGVF and Mexico City region, we propose that before 3 Ma the slab geometry in the MGVF resembled that of the Mexico City region today. To account for this change in slab geometry over time, we used two 2-D thermal models to look at production of subduction-related H_2O-rich components: (1) using the current slab geometry (Fig. 18); (2) using the inferred flat-slab geometry at 3 Ma (Fig. 19).

Dehydration of subducted material—present-day slab configuration

Based on the thermal structure calculated for the present-day slab geometry, the volcanic front region of the MGVF corresponds to subducted slab depths of $\sim$80 km and maximum slab surface temperatures (SST) of $\sim$600–700°C (Fig. 18). Maximum temperatures in the wedge beneath the volcanic front (1200–1300°C at $\sim$2 GPa) agree well
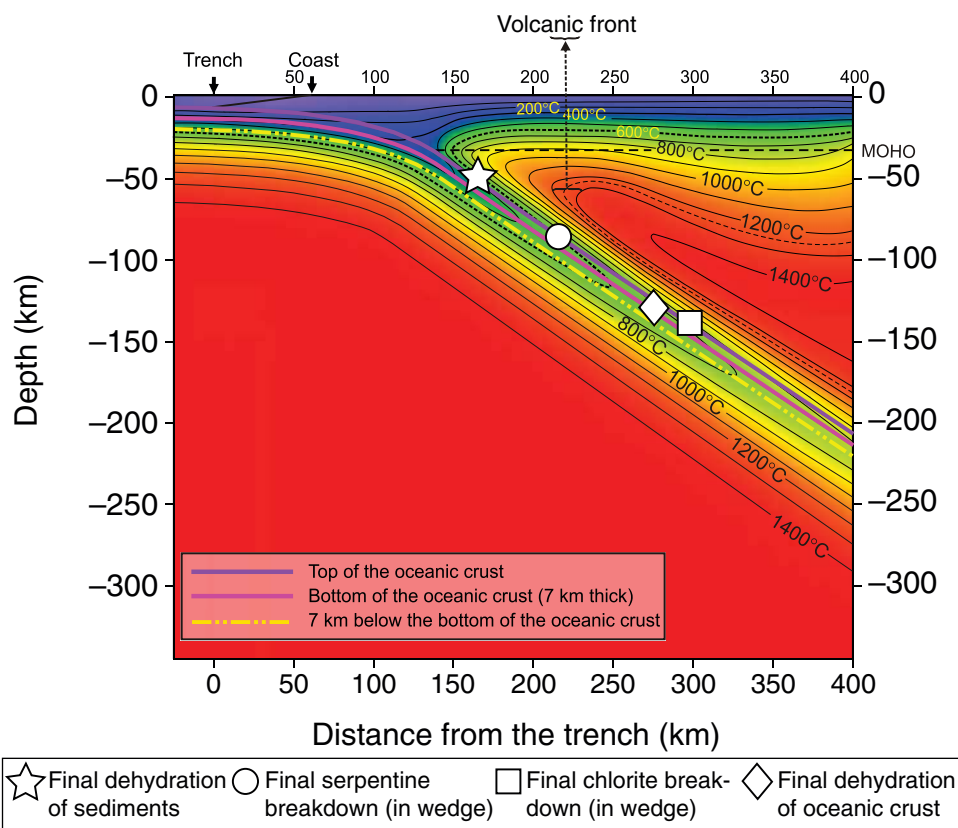
Fig. 18. A 2-D thermal model of the subduction zone beneath the MGVF from the Middle America Trench to 400 km from the trench. The volcanic front is located above the region where the mantle wedge temperatures reach 1200–1300°C (dashed arrow). Symbols indicate the depths and temperatures at which key fluid release processes should reach completion.

with the estimates based on primitive melt H_2O contents and estimated extents of melting (Fig. 14). The region far behind the front (350 km from the trench) corresponds to slab depths of ∼170 km and maximum SSTs of ∼850°C, although we emphasize that the depth to the slab in this region is not constrained by seismic data.

Using the P–T conditions predicted for the subducting oceanic lithosphere and phase diagrams for altered oceanic crust, serpentinized mantle, and sediment (Rüpke *et al.*, 2004), we predicted where H_2O should be released from the subducted slab. The average composition of Cocos plate sediment is reasonably similar to the GLOSS global sediment average (Plank & Langmuir, 1998) used by Rüpke *et al.* (2004), so their calculated phase relations should be appropriate for sediment subduction beneath the MGVF. We assumed vertical rise of fluids from the slab, but real patterns of fluid ascent are likely to be more complex (e.g. Schurr *et al.*, 2003; Cagnioncle *et al.*, 2007). Based on the predicted P–T conditions in the slab and mantle wedge and calculated phase equilibria for metasediment, the subducted sediment should release most of its H_2O beneath the forearc region (Figs 18 and 20a), though some H_2O could be carried deeper by phengite (Herman

& Spandler, 2008). Based on temperatures for the upper part of the slab, dehydration of the uppermost 3 km of oceanic crust (where most of the H_2O is stored; Rüpke *et al.*, 2004) should be largely complete by depths of ∼120–130 km (Fig. 20a), which corresponds to regions ∼50 km behind the volcanic front. This dehydration depth appears to be at odds with the correlation between the maximum depth of earthquakes in subducting slabs and the blueschist to eclogite transition (Rondenay *et al.*, 2008), as the data of Pardo & Suárez (1995) indicate that the subducting Cocos plate lacks seismic events at depths >70 km. However, recent seismic data for the Cocos plate just west of the MGVF show that intra-slab earthquakes occur to a depth of ∼120 km (Fig. 7 of Yang *et al.*, 2009, fig. 7, profile A4–B4), consistent with our predicted depth of final dehydration for the altered oceanic crust.

A major complication to understanding the transfer of H_2O-rich components from the slab to the melting zone in the hot part of the mantle wedge is the stability of hydrous phases in peridotite. Down-dragging of the hydrated mantle wedge as a result of corner flow may aid in transferring hydrous phases to greater depths (Tatsumi & Eggins, 1995). Recent experimental work by Grove *et al.* (2006)
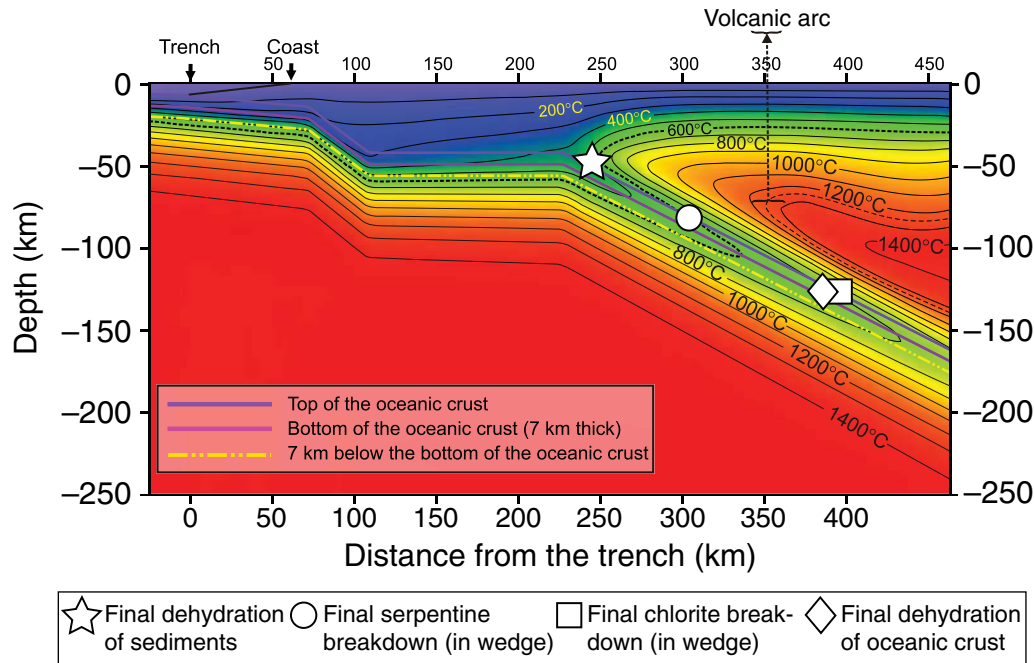
Fig. 19. A 2-D thermal model of the subduction zone beneath the MGVF at 3 Ma. Symbols as in Fig. l8.

suggested that fluids released at lower pressures and temperatures into the mantle wedge will react with peridotite to form chlorite-bearing peridotite (with ≤l2 wt % H_2O) that is coupled with the plate and dragged to higher pressures and temperatures where eventual breakdown of chlorite releases fluid. The stability of this phase to 850°C at ∼3 GPa may expand the zone over which hydrous melts can be produced in the mantle wedge (Grove *et al.*, 2006). Similar arguments have been made for the role of serpentine in peridotite in the mantle wedge just above the slab (Wysoczanski *et al.*, 2006), although the maximum temperature of this phase does not allow it to carry H_2O as deep as chlorite.

The upper stability limits for serpentine and chlorite in the overlying mantle wedge are shown in Fig. l8. Dehydration of subducted sediment and altered oceanic crust beneath the forearc region should release fluids into the overlying mantle wedge, where mantle peridotite would react with the fluids to form serpentinite. This hydrated material would be dragged down with the slab, and eventually the serpentine would break down at depths of <l00 km and temperatures of ∼600°C (Rüpke *et al.*, 2004). However, the fluids released by this breakdown could be incorporated into chlorite in the mantle wedge (continued fluxing from the slab would augment chlorite formation as well), which would continue its slab-coupled movement to greater depths until the breakdown of chlorite at ∼750–800°C and ∼4 GPa (Pawley, 2003; Grove *et al.*, 2006). The stability of chlorite to these depths would

allow production of hydrous fluids in the mantle beneath the region extending to ∼75 km behind the volcanic front in the MGVF (Fig. 20a). This is similar to the region that is directly fluxed by the waning stages of H_2O release from subducted oceanic crust. However, there is still a significant portion of the MGVF at distances >75 km behind the front with high magmatic H_2O contents that still cannot be explained by these mechanisms (Fig. ll).

The strong correlation between H_2O and Cl in the MGVF primitive melts (Fig. 8) supports the role of a single phase, such as serpentine or chlorite, controlling the fluids released into the mantle wedge. Studies of serpentinite suggest that the salinities of fluids released during serpentinite breakdown range from 4 to 8 wt % NaCl (Scambelluri *et al.*, 2004), which overlaps with the MGVF data. The salinity of fluids related to chlorite breakdown is unknown, but the fluids released by serpentine breakdown could potentially be incorporated into chlorite and may thus retain similar Cl/H_2O ratios. The MGVF Cl/H_2O data are also very similar to the salinities of fluids released from the upper oceanic crust (∼4 wt % NaCl; Philippot *et al.*, l998).

Another potential mechanism of fluid release from the slab at great depth involves the breakdown of serpentinite in the subducting oceanic lithosphere (Rüpke *et al.*, 2002; Schmidt & Poli, 2004; Spandler *et al.*, 2008). Seismic velocities suggest that the subducting Cocos plate beneath Nicaragua is unusually H_2O-rich (Abers *et al.*, 2003). Such hydration may be linked to extensive fracturing of the
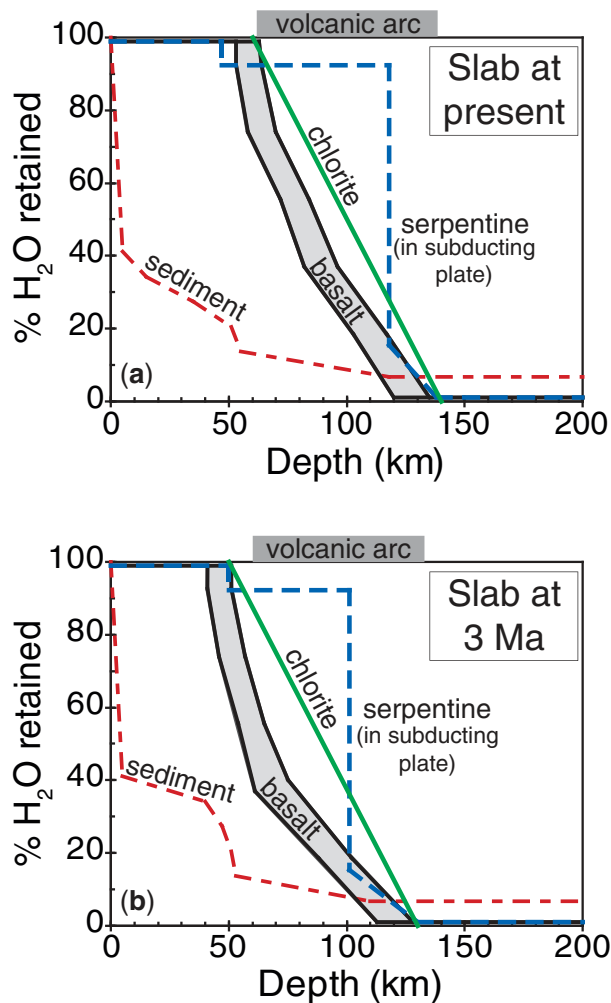
Fig. 20. Calculated per cent of initial H_2O that is retained in subducted sediment, oceanic crust, and serpentinized mantle in the downgoing plate vs depth in the present slab configuration (a) and for the slab at 3 Ma (b). Lines for chlorite indicate the range of depths over which chlorite in the lowermost mantle wedge should dehydrate, assuming that the lowermost wedge is dragged downwards along with the subducted plate.

oceanic crust at the outer rise prior to subduction that allowed seawater to penetrate, resulting in crustal hydration and conversion of the mantle in the subducting slab to serpentinite (Rüpke *et al.*, 2002; Abers *et al.*, 2003). Rüpke *et al.* (2002) showed that serpentinite in the slab beneath Nicaragua is stable to high pressures, releasing its H_2O at depths of 130–160 km. Fluids released by serpentinite breakdown should have low $\delta^{18}O$, and Nicaraguan magmas have $\delta^{18}O_{olivine}$ values (4·6–5·2‰) that are lower than normal mantle values (Eiler *et al.*, 2005). Furthermore, fluids released from the breakdown of serpentinite typically have high fluid-mobile element concentrations (Tenthorey & Hermann, 2004), and magmas in Nicaragua have high Ba/La ratios (Fig. 3; Eiler *et al.*, 2005), though this latter characteristic could also be

caused by the distinctly high Ba content of subducted carbonate sediment in this region (Patino *et al.*, 2000). Given the high $\delta^{18}O_{olivine}$ and low Ba/La values for MGVF magmas and the lack of evidence for pervasive serpentinization of the Cocos plate offshore of Mexico, we conclude that serpentinite breakdown in the subducted slab is unlikely to be the source of H_2O-rich components beneath the MGVF.

To summarize the models discussed above, dehydration of the oceanic crust begins beneath the forearc region but continues beneath the volcanic front and behind the front for ~50–75 km distance, and down-dragging of chloritized mantle can augment this fluid flux to ~75 km behind the front (Fig. 20a). However, the high $\delta^{18}O$ values and trace element compositions of the MGVF primitive magmas and modeled subduction components suggest involvement of sediment melts. To melt subducted sediment beneath the volcanic arc, fluid fluxing is required to lower the melting temperature of the metasediments, which would have dehydrated when they were beneath the forearc (Fig. 20a). Because the subducted upper oceanic crust continues dewatering to ~120–130 km depth, the percolation of fluids from the oceanic crust into the overlying dehydrated metasediments should induce sediment melting (based on wet solidus temperatures for subducted sediment of ~650–800°C; Nicholls *et al.*, 1996; Hermann & Spandler, 2008). The rising sediment melt may in turn melt the overlying hydrated (chlorite-bearing) mantle wedge (chlorite is stable along the wet-peridotite solidus above ~2 GPa; Grove *et al.*, 2006), or the sediment melts may mix with fluids being released from chlorite breakdown if temperatures in the wedge are ≥750–800°C. Either scenario can produce the high-H_2O, high-$\delta^{18}O$ subduction component with both sediment melt and altered oceanic crust-derived fluid components (Fig. 16). However, it does not appear possible with the current plate geometry to generate high-H_2O, high-$\delta^{18}O$ magmas beyond slab depths of ~130 km (distances >~75 km behind the volcanic front).

Dehydration of subducted material—3 Ma

Following our assumption of a flat-slab geometry at 3 Ma, a second 2-D thermal model was created for the MGVF (Fig. 19). In this model, the volcanic front would have been located about 350 km from the present-day trench based on peak mantle wedge temperatures of 1200–1300°C beneath this region. Using the same $P-T$ phase diagrams for metasediment and metabasalt dehydration (Rüpke *et al.*, 2004) in this configuration, subducted sediment would have mostly dehydrated by ~50 km depth (Fig. 20b), at which depth the top of the slab would have been ~250 km from the present-day trench. Dehydration of the upper part of the altered oceanic crust would have begun beneath the forearc and would have continued beneath the volcanic front at 3 Ma (~350 km from the trench), with dehydration reaching completion in the

region $\sim$375–400 km from the trench (top of the subducted plate at $\sim$110–130 km depth). As discussed above for the present-day plate configuration, fluids released from the oceanic crust at these depths could also have melted the overlying dehydrated metasediment package. Thus, the slab geometry at 3 Ma would have allowed production of sediment melts and hydrous, oceanic-crust-derived fluids at the high-H_2O localities located far behind the volcanic front today. Additionally, the stability fields for chlorite in the mantle wedge in the flat-slab configuration suggest that fluids would have been produced in the lowermost mantle wedge by chlorite breakdown over the same region (volcanic front at 3 Ma to $\sim$50 km behind the front). The combination of these processes could have resulted in hydration of the mantle wedge and formation of H_2O-rich magmas in the region that is far behind the present-day volcanic front.

Unfortunately, it is not possible to definitively resolve the influence of slab migration on the generation of hydrous melts across the MGVF. Although much of the volcanism at 3 Ma was concentrated in the region far behind the present-day volcanic front, it is also clear that activity in this region has persisted into recent times. A compilation of ages determined for MGVF cinder cones (Hasenaka & Carmichael, 1985; Ban *et al.*, 1992; Suter *et al.*, 2001; Ownby *et al.*, 2007) suggests that most of the volcanic activity younger than 1 Ma is located near the region of the current volcanic front. However, there is wide variability in the ages of cinder cones across the arc. Volcanoes far behind the front have been active as recently as $\sim$50 ka BP (Suter *et al.*, 2001), and most of the alkali basalt maars and tuff rings in the Valle de Santiago region far behind the volcanic front are $\leq$0·38 Ma in age (Uribe-Cifuentes & Urrutia-Fucugauchi, 1999). Thus, it is likely that at least some of the volatile-rich magmas erupted far behind the front at 2–3 Ma when the slab was shallower or moving trenchward. However, it is also possible that some of the volatile-rich magmas far behind the front erupted more recently, produced by melting of previously hydrated mantle; additional geochronological work is needed to assess these possibilities. Whether or not volcanoes near the current volcanic front are tapping mantle that was hydrated at 2–3 Ma when this region was above the forearc is difficult to ascertain. The geometry of the slab in the 3 Ma model (based on the present-day configuration near Mexico City) is flat and shallow until $\sim$250 km from the trench. The flat-slab region south of Mexico City has at most a 10$\pm$3 km thick low-velocity zone, which could represent a hydrated mantle wedge remnant, between the base of the continental crust and the top of the subducted oceanic plate (Perez-Campos *et al.*, 2008). Thus there is little room for mantle lithosphere and no mantle asthenosphere between the upper and lower plates (Perez-Campos *et al.*, 2008). Based on this geometry, the amount

of hydrated forearc mantle that could have formed at 2–3 Ma beneath the region of the MGVF that is now the volcanic front is limited compared with forearcs like that in Cascadia, which has a thicker zone of hydrated forearc mantle (Brocher *et al.*, 2003).

The change in slab geometry over the past 3 Ma has important implications for mantle flow and production of melts by decompression. Trenchward migration of subducting slabs creates suction in the mantle wedge, which would increase the corner flow of mantle from far behind the arc. Melting of this mantle, which has not undergone previous fluid-flux melting, would yield OIB-type magmas that have high HFSE and low H_2O concentrations. This advection of mantle has been suggested to produce alkaline, decompression melts in the western TMVB (Luhr, 1997) and to the east in the CVF (Wallace & Carmichael, 1999). This model is consistent with the presence of low-H_2O, low-degree partial melts far behind the front in the MGVF (e.g. Hoya Alvarez). The range of low to moderate magmatic H_2O contents in the NE part of the MGVF (Fig. 11) may indicate a mantle region that was fluxed by slab components at 2–3 Ma but is now dominated by decompression melting related to the trenchward migration of the Cocos slab over the past 2 Myr. Our model results for the flat-slab geometry at 3 Ma and the presence of more H_2O-rich magmas in the region well behind the current volcanic front have important implications for the Laramide orogeny in the western USA, as they demonstrate that a flat-slab plate configuration can transport H_2O far into plate interiors (e.g. Humphreys *et al.*, 2003).

CONCLUSIONS

Despite the young age of the subducting Cocos plate, primary calc-alkaline magmas in the MGVF have high concentrations of H_2O (3–5·8 wt %) and other volatiles across large distances ($\sim$150 km) behind the volcanic front. Additionally, $\delta^{18}O_{olivine}$ values measured for the MGVF (5·6–6‰) are higher than values in Central America and most other arcs worldwide. MGVF calc-alkaline magmas originated from an OIB mantle source that was variably depleted by previous partial melting and melt extraction (PME) and later remelted by fluxing of H_2O-rich components derived from the subducted slab. Models based on trace elements and volatiles (i.e. H_2O) suggest magma formation by 6–15% partial melting of mantle sources that had mostly experienced 0–3% PME, although the source for one cone (Jorullo) required 10% PME. These melt fractions and the melt H_2O contents indicate mantle temperatures that are 40–50°C lower than the dry peridotite solidus. In contrast to the calc-alkaline magmas, H_2O-poor alkali basaltic magmas formed by small degrees of decompression melting of an OIB source that had not been fluxed by slab-derived components.

The amounts and compositions of H_2O-rich components added to the mantle wedge beneath the MGVF are similar to those estimated for Central America and Kamchatka despite large differences in subducted plate age and the thickness and composition of subducted sediment in these arcs. Based on high $\delta^{18}O_{olivine}$ values and relatively high Th, La, and Ba contents, the H_2O-rich subduction components added to the mantle wedge beneath the MGVF are likely to be mixtures of oceanic crust-derived fluids and sediment melts.

Using 2-D thermo-mechanical models to constrain slab dehydration and sediment melting, we demonstrate that the present-day plate configuration beneath the MGVF causes fluids to be released beneath the forearc and volcanic front. The formation of sediment melts beneath the volcanic front is probably linked to the waning stages of fluid release from the oceanic crust, which results in fluid percolation through already dehydrated sediments. H_2O-rich magmas located more than ~50 km behind the volcanic front can be explained by mantle hydration related to a shallower slab geometry that existed at ~3 Ma. The flat-slab geometry would have allowed production of H_2O-rich, high-$\delta^{18}O$ magmas far behind the current volcanic front, demonstrating that flat-slab subduction can transport H_2O into the mantle underlying plate interiors far from a plate boundary.

ACKNOWLEDGEMENTS

SUPPLEMENTARY DATA

Supplementary data for this paper are available at *Journal of Petrology* online.

REFERENCES

Abers, G. A., Plank, T. & Hacker, B. R. (2003). The wet Nicaraguan slab. *Geophysical Research Letters* **30**, doi:l0.1029/2992GL015649.

Alt, J. C. & Shanks, W. C. III. (2006). Stable isotope compositions of serpentinite seamounts in the Mariana forearc: Serpentinization processes, fluid sources and sulfur metasomatism. *Earth and Planetary Science Letters* **242**, 272–285.

Alt, J. C., Muehlenbacks, K. & Honnorex, J. (1986). An oxygen isotopic profile through the upper kilometer of the oceanic crust, DSDP hole 504B. *Earth and Planetary Science Letters* **80**, 217–229.

Anderson, A. T. (1982). Parental basalts in subduction zones: implications for continental evolution. *Journal of Geophysical Research* **87**, 7047–7060.

Arthur, M. A., Anderson, T. F. & Kaplan, I. R. (1983). *Stable Isotopes in Sedimentary Geology. SEPM Short Course* **10**, 432 pp.

Auer, S. L., Bindeman, I. N., Wallace, P. J., Ponomareva, V. V. & Portnyagin, M. V. (2009). The origin of hydrous, high-$\delta^{18}O$ voluminous volcanism: Diverse oxygen isotope values and high magmatic water contents with the volcanic record of Klyuchevskoy volcano, Kamchatka, Russia. *Contributions to Mineralogy and Petrology* **157**, 209–230.

Ban, M., Hasenaka, T., Delgado-Granados, H. & Takaoka, N. (1992). K–Ar ages of lavas from shield volcanoes in the Michoacán–Guanajuato volcanic field, Mexico. *Geofisica Internacional* **31**, 467–473.

Benjamin, E. R., Plank, T., Wade, J. A., Kelley, K. A., Hauri, E. H. & Alvarado, G. E. (2007). High water contents in basaltic magmas from Irazú Volcano, Costa Rica. *Journal of Volcanology and Geothermal Research* **168**, 68–92, doi:l0.l0l6/j.jvolgeores.2007.08.008.

Bindeman, I. (2008). Oxygen isotopes in mantle and crustal magmas as revealed by single crystal analysis. In: Putirka, K. D. & Tepley III, F. J. (eds) *Minerals, inclusions and volcanic processes, Reviews in Mineralogy and Geochemistry, Mineralogical Society of America* **69**, 445–478.

Bindeman, I. N., Ponomareva, V. V., Bailey, J. C. & Valley, J. W. (2004). Volcanic arc of Kamchatka: a province with high-$\delta^{18}O$ magma sources and large-scale $^{18}O/^{16}O$ depletion of the upper crust. *Geochimica et Cosmochimica Acta* **68**, 841–865.

Bindeman, I. N., Eiler, J. M., Yogodzinski, G., Tatsumi, Y., Stern, C., Grove, T., Portnyagin, M., Hoernle, K. & Danyushevsky, L. (2005). Oxygen isotope evidence for slab melting in modern and ancient subduction zones. *Earth and Planetary Science Letters* **235**, 480–496.

Blatter, D. L., Carmichael, I. S. E., Deino, A. L. & Renne, P. R. (2001). Neogene volcanism at the front of the central Mexican volcanic belt: Basaltic andesites to dacites, with contemporaneous shoshonites and high-TiO_2 lava. *Geological Society of America Bulletin* **113**, 1324–1342.

Blatter, D. L., Farmer, G. L. & Carmichael, I. S. E. (2007). A north–south transect across the Central Mexican Volcanic Belt at ~100°W: Spatial distribution, petrological, geochemical, and isotopic characteristics of Quaternary volcanism. *Journal of Petrology* **48**, 901–950.

Brocher, T. M., Parsons, T., Trehu, A. M., Snelson, C. M. & Fisher, M. A. (2003). Seismic evidence for widespread serpentinized forearc upper mantle along the Cascadia margin. *Geology* **31**, 267–270.

Cagnioncle, A. M., Parmentier, E. M. & Elkins-Tanton, L. T. (2007). Effect of solid flow above a subducting slab on water distribution and melting at convergent plate boundaries. *Journal of Geophysical Research* **112**, doi:l0.1029/2007JB004934.

Cervantes, P. & Wallace, P. J. (2003). Role of H_2O in subduction-zone magmatism: New insights from melt inclusions in high-Mg basalts from central Mexico. *Geology* **31**, 235–238.

Danyushevsky, L. V., Della-Pasqua, F. N. & Sokolov, S. (2000). Re-equilibration of melt inclusions trapped by magnesian olivine phenocrysts from subduction-related magmas: Petrological implications. *Contributions to Mineralogy and Petrology* **138**, 68–83.

DeMets, C., Gordon, R., Argus, D. & Stein, S. (1994). Effect of recent revisions to the geomagnetic reversal time scale on estimates of current plate motions. *Geophysical Research Letters* **21**, 2191–2194.

Dixon, J. E. & Pan, V. (1995). Determination of the molar absorptivity of dissolved carbonate in basanitic glass. *American Mineralogist* **80**, 1339–1342.

Dixon, J. E., Stolper, E. M. & Holloway, J. R. (1995). An experimental study of water and carbon dioxide solubilities in mid-ocean ridge

basaltic liquids. Part I: Calibration and solubility models. *Journal of Petrology* **36**, 1607–1631.

Dixon, J. E., Clague, D. A., Wallace, P. & Poreda, R. (1997). Volatiles in alkalic basalts from the North Arch volcanic field, Hawaii: Extensive degassing of deep submarine-erupted alkalic series lavas. *Journal of Petrology* **38**, 911–939.

Dorendorf, F., Wiechert, U. & Wörner, G. (2000). Hydrated sub-arc mantle: a source for the Kluchevskoy volcano, Kamchatka/Russia. *Earth and Planetary Science Letters* **175**, 69–86.

Eiler, J. M. (2001). Oxygen isotope variations of basaltic lavas and upper mantle rocks. In: Valley, J. W. & Cole, D. R. (eds) *Stable Isotope Geochemistry. Mineralogical Society of America, Reviews in Mineralogy and Geochemistry* **43**, 319–364.

Eiler, J. M., Crawford, A., Elliott, T., Farley, K. A., Valley, J. W. & Stolper, E. M. (2000). Oxygen isotopic geochemistry of oceanic arc lavas. *Journal of Petrology* **41**, 229–256.

Eiler, J. M., Carr, M. J., Reagan, M. & Stolper, E. (2005). Oxygen isotope constraints on the sources of Central American arc lavas. *Geochemistry, Geophysics, Geosystems* **6**, Q07007, doi:10.1029/2004GC000804.

Ferrari, L. (2004). Slab detachment control on mafic volcanic pulse and mantle heterogeneity in central Mexico. *Geology* **32**, 77–80.

Ferrari, L., Lopez-Martinez, M., Aguirre-Diaz, G. & Carrasco-Nuñez, G. (1999). Space–time patterns of Cenozoic arc volcanism in central Mexico: from the Sierra Madre Occidental to the Mexican Volcanic Belt. *Geology* **27**, 303–306.

Fyfe, W. S. & McBirney, A. R. (1975). Subduction and structure of andesitic volcanic belts. *American Journal of Science* **A275**, 285–297.

Gaetani, G. A. & Grove, T. L. (1998). The influence of water on melting of mantle peridotite. *Contributions to Mineralogy and Petrology* **131**, 323–346.

Gaetani, G. A., Grove, T. L. & Bryan, W. B. (1993). The influence of water on the petrogenesis of subduction-related igneous rocks. *Nature* **365**, 332–334.

Gaetani, G. A., Kent, A. J. R., Grove, T. L., Hutcheon, I. D. & Stolper, E. M. (2003). Mineral/melt partitioning of trace elements during hydrous peridotite partial melting. *Contributions to Mineralogy and Petrology* **145**, 391–405.

Ghiorso, M. S. & Sack, R. O. (1995). Chemical mass transfer in magmatic processes. IV. A revised and internally consistent thermodynamic model for the interpolation and extrapolation of liquid–solid equilibria in magmatic systems at elevated temperatures and pressures. *Contributions to Mineralogy and Petrology* **119**, 197–212.

Gomez-Tueña, A., Langmuir, C. H., Goldstein, S. L., Straub, S. M. & Ortega-Gutierrez, F. (2007). Geochemical evidence for slab melting in the Trans-Mexican Volcanic Belt. *Journal of Petrology* **48**, 537–562.

Grove, T., Parman, S., Bowring, S., Price, R. & Baker, M. (2002). The role of an H_2O-rich fluid component in the generation of primitivie basaltic andesites and andesites from the Mt. Shasta region, N California. *Contributions to Mineralogy and Petrology* **142**, 375–396.

Grove, T. L., Chatterjee, N., Parman, S. W. & Médard, E. (2006). The influence of H_2O on mantle wedge melting. *Earth and Planetary Science Letters* **249**, 74–89, doi:10.1016/j.epsl.2006.06.043.

Gurenko, A. A., Belousov, A. B., Trumbull, R. B. & Sobolev, A. V. (2005). Explosive basaltic volcanism of the Chikurachki Volcano (Kurile arc, Russia): Insights on pre-eruptive magmatic conditions and volatile budget revealed from phenocryst-hosted melt inclusions and groundmass glasses. *Journal of Volcanology and Geothermal Research* **147**, 203–232.

Harmon, R. S. & Hoefs, J. (1995). Oxygen isotope heterogeneity of the mantle deduced from global [18]O systematics of basalts from different geotectonic settings. *Contributions to Mineralogy and Petrology* **120**, 95–114.

Hasenaka, T. & Carmichael, I. S. E. (1985). The cinder cones of Michoacan–Guanajuato, central Mexico: Their age, volume and distribution and magma discharge rate. *Journal of Volcanology and Geothermal Research* **25**, 105–124.

Hasenaka, T. & Carmichael, I. S. E. (1987). The cinder cones of Michoacán–Guanajuato, central Mexico: Petrology and chemistry. *Journal of Petrology* **28**, 241–269.

Hauri, E. H., Gaetani, G. A. & Green, T. H. (2006). Partitioning of water during melting of the Earth's upper mantle at H_2O-saturated conditions. *Earth and Planetary Science Letters* **248**, 715–734.

Hermann, J. & Spandler, C. J. (2008). Sediment melts at sub-arc depths: An experimental study. *Journal of Petrology* **49**, 717–740.

Hirschmann, M. M., Aubaud, C. & Withers, A. C. (2005). Storage capacity of H_2O in nominally anhydrous minerals in the upper mantle. *Earth and Planetary Science Letters* **236**, 167–181.

Hochstaedter, A. G., Ryan, J. G., Luhr, J. F. & Hasenaka, T. (1996). On B/Be ratios in the Mexican Volcanic Belt. *Geochimica et Cosmochimica Acta* **60**, 613–628.

Humphreys, E., Hessler, E., Dueker, K., Farmer, G. L., Erslev, E. & Atwater, T. (2003). How Laramide-age hydration of North American lithosphere by the Farallon slab controlled subsequent activity in the Western United States. *International Geology Review* **45**, 575–595.

John, T., Klemd, R., Gao, J. & Garbe-Schönberg, C-D. (2008). Trace-element mobilization in slabs due to non steady-state fluid-rock interaction: Constraints from an eclogite-facies transport vein in blueschist (Tianshan, China). *Lithos* **103**, 1–24.

Johnson, E. R., Wallace, P. J., Cashman, K. V., Delgado Granados, H. & Kent, A. J. (2008). Magmatic volatile contents and degassing-induced crystallization at Volcán Jorullo, Mexico: Implications for melt evolution and the plumbing systems of monogenetic volcanoes. *Earth and Planetary Science Letters* **269**, 477–486, doi:10.1016/j.epsl.2008.03.004.

Johnson, E. R., Wallace, P. J., Cashman, K. V. & Delgado Granados, H. (2009). Degassing of volatiles (H_2O, CO_2, S, Cl) during ascent, crystallization, and eruption of basaltic magmas. *Journal of Volcanology and Geothermal Research* (in press).

Katz, R. F., Spiegelman, M. & Langmuir, C. H. (2003). A new parameterization of hydrous mantle melting. *Geochemistry, Geophysics, Geosystems* **4**, doi:10.1029/2002GC000433.

Kelley, K. A., Plank, T., Grove, T. L., Stolper, E. M., Newman, S. & Hauri, E. (2006). Mantle melting as a function of water content beneath back-arc basins. *Journal of Geophysical Research* **111**, B09208, doi:10.1029/2005JB003732.

Kent, A. J. R., Peate, D. W., Newman, S., Stolper, E. M. & Pearce, J. A. (2002). Chlorine in submarine glasses from the Lau Basin: seawater contamination and constraints on the composition of slab-derived fluids. *Earth and Planetary Science Letters* **202**, 361–377.

Kent, A. J. R., Stolper, E. M., Francis, D., Woodhead, J., Frei, R. & Eiler, J. (2004). Mantle heterogeneity during the formation of the North Atlantic Tertiary Province: Constraints from trace element and Sr–Nd–Os–O isotope systematics of Baffin Island picrites. *Geochemistry, Geophysics, Geosystems* **5**, Q11004, doi:10.1029/2004GC000743.

Kerrick, D. M. & Connolly, J. A. D. (2001). Metamorphic devolatilization of subducted marine sediments and the transport of volatiles into the Earth's mantle. *Nature* **411**, 293–296.

Kessel, R., Schmidt, M. W., Ulmer, P. & Pettke, T. (2005). Trace element signature of subduction-zone fluids, melts and supercritical liquids at 120–180 km depth. *Nature* **437**, doi:10.0038/nature03971.

Kirby, S. H., Engdahl, E. R. & Villaseñor, A. (2002). Warm-slab subduction as a global process. In: Kirby, S. H., Wang, K. & Dunlop, S. G. (eds) *The Cascadia Subduction Zone and Related*

Subduction systems. US Geological Survey Open-File Report **02-328**, 223–276.

Kolodny, Y. & Epstein, S. (1976). Stable isotope geochemistry of deep-sea cherts. *Geochimica et Cosmochimica Acta* **40**, 1195–1209.

Kress, V. C. & Carmichael, I. S. E. (1991). The compressibility of silicate liquids containing Fe_2O_3 and the effect of composition, temperature, oxygen fugacity and pressure on their redox states. *Contributions to Mineralogy and Petrology* **108**, 82–92.

Lagatta, A. (2003). Arc magma genesis in the eastern Mexican volcanic belt. Ph.D. thesis, Columbia University, New York.

le Roux, P. J., Shirey, S. B., Hauri, E. H., Perfit, M. R. & Bender, J. F. (2006). The effects of variable sources, processes and contaminants on the composition of northern EPR MORB (8–10°N and 12–14°N): Evidence from volatiles (H_2O, CO_2, S) and halogens (F, Cl). *Earth and Planetary Science Letters* **251**, 209–231.

Luhr, J. F. (1992). Slab-derived fluids and partial melting in subduction zones: insights from two contrasting Mexican volcanoes (Colima and Ceboruco). *Journal of Volcanology and Geothermal Research* **54**, 1–18.

Luhr, J. F. (1997). Extensional tectonics and the diverse primitive volcanic rocks in the western Mexican volcanic belt. *Canadian Mineralogist* **35**, 473–500.

Luhr, J. F. (2001). Glass inclusions and melt volatile contents at Parícutin Volcano, Mexico. *Contributions to Mineralogy and Petrology* **142**, 261–283.

Luhr, J. F. & Carmichael, I. S. E. (1985). Jorullo volcano, Michoacán, Mexico (1759–1774): The earliest stages of fractionation in calc-alkaline magmas. *Contributions to Mineralogy and Petrology* **90**, 142–161.

Luhr, J. F., Allan, J. F., Carmichael, I. S. E., Nelson, S. A. & Hasenaka, T. (1989). Primitive calc-alkaline and alkaline rock types form the western Mexican Volcanic Belt. *Journal of Geophysical Research* **94**, 4515–4530.

Manea, M., Manea, V. C. & Kostoglodov, V. (2003). Sediment fill in the Middle America Trench inferred from gravity anomalies. *Geofisica Internacional* **42**, 603–612.

Manea, V. C., Manea, M., Kostoglodov, V., Currie, C. & Sewell, G. (2004). Thermal structure, coupling and metamorphism in the Mexican subduction zone beneath Guerrero. *Geophysical Journal International* **58**, 775–784.

Manea, V. C., Manea, M., Kostoglodov, V. & Sewell, G. (2005). Thermo-mechanical model of the mantle wedge in Central Mexican subduction zone and a blob tracing approach for the magma transport. *Earth and Planetary Science Letters* **149**, 165–186.

Manea, V., Manea, M., Kostoglodov, V. & Sewell, G. (2006). Intra-slab seismicity and thermal stress in the subducted Cocos plate beneath central Mexico. *Tectonophysics* **420**, 389–408.

Martin, E., Bindeman, I. N. & Grove, T. L. (2009). Ancient and modern subduction $\delta^{18}O$ signature of the mantle wedge: across-arc geochemical study of Mt. Shasta and Medicine Lake volcanoes (California). *Contributions to Mineralogy and Petrology* (in press).

Mattey, D., Lowry, D. & Macpherson, C. (1994). Oxygen isotope composition of mantle peridotite. *Earth and Planetary Science Letters* **128**, 231–241.

McBirney, A. R. (1969). Compositional variations in Cenozoic calc-alkaline suites of Central America. In: McBirney, A. R. (ed.) *Proceedings of the Andesite Converence.* Portland, OR: State of Oregon, Department of Geology and Mineral Industries, pp. 185–189.

McCulloch, M. T. & Gamble, J. A. (1991). Geochemical and geodynamical constraints on subduction zone magmatism. *Earth and Planetary Science Letters* **102**, 358–374.

McDonough, W. F. & Sun, S. S. (1995). The composition of the Earth. *Chemical Geology* **120**, 223–253.

McMillan, N. J., Dickin, A. P. & Haag, K. (2000). Evolution of magma source regions in the Rio Grande rift, southern New Mexico. *Geological Society of America Bulletin* **112**, 1582–1593.

Métrich, N. & Wallace, P. J. (2008). Volatile abundances in basaltic magmas and their degassing paths tracked by melt inclusions. In: Putirka, K. D. & Tepley III, F. J. (eds) *Minerals, inclusions and volcanic processes, Reviews in Mineralogy and Geochemistry, Mineralogical Society of America* **69**, 363–402.

Mukasa, S. B., Blatter, D. L. & Andronikov, A. V. (2007). Mantle peridotite xenoliths in andesite lava at El Peñon, central Mexican Volcanic Belt: Isotopic and trace element evidence for melting and metasomatism in the mantle wedge beneath an active arc. *Earth and Planetary Science Letters* **260**, 37–55.

Nichols, G. T., Wyllie, P. J. & Stern, C. R. (1996). Experimental melting of pelagic sediment: Constraints relevant to subduction. In: Bebout, G. E., Scholl, D. W., Kirby, S. H. & Platt, J. P. (eds) *Subduction: Top to Bottom. Geophysical Monograph, American Geophysical Union* **96**, 293–298.

Ownby, S., Delgado Granados, H., Lange, R. A. & Hall, C. M. (2007). Volcan Tancitaro, Michoacan, Mexico, $^{40}Ar/^{39}Ar$ constraints on its history of sector collapse. *Journal of Volcanology and Geothermal Research* **161**, 1–14.

Pardo, M. & Suárez, G. (1995). Shape of the subducted Rivera and Cocos plates in southern Mexico: seismic and tectonic implications. *Journal of Geophysical Research* **100**, 12357–12373.

Patino, L. C., Carr, M. J. & Feigensen, M. D. (2000). Local and regional variations in Central American arc lavas controlled by variations in subducted sediment input. *Contributions to Mineralogy and Petrology* **138**, 265–283.

Pawley, A. (2003). Chlorite stability in mantle peridotite: The reaction clinochlore + enstatite = forsterite + pyrope + H_2O. *Contributions to Mineralogy and Petrology* **144**, 449–456.

Pearce, J. A. & Peate, D. W. (1995). Tectonic implications of the composition of volcanic arc magmas. *Annual Review of Earth and Planetary Sciences* **23**, 251–285.

Perez-Campos, X., Kim, Y. H., Husker, A., Davis, P. M., Clayton, R. W., Iglesias, A., Pacheco, J. F., Singh, S. K., Manea, V. C. & Gurnis, M. (2008). Horizontal subduction and truncation of the Cocos Plate beneath central Mexico. *Geophysical Research Letters* **35**, doi:10.1029/2008GL035127.

Philippot, P., Agrinier, P. & Scambelluri, M. (1998). Chlorine cycling during subduction of altered oceanic crust. *Earth and Planetary Science Letters* **161**, 33–44.

Plank, T. (2005). Constraints from thorium/lanthanum on sediment recycling at subduction zones and the evolution of the continents. *Journal of Petrology* **46**, 921–944.

Plank, T. & Langmuir, C. H. (1998). The chemical composition of subducting sediment and its consequences for the crust and mantle. *Chemical Geology* **143**, 325–394.

Portnyagin, M., Hoernle, K., Plechov, P., Mironov, N. & Khubunaya, S. (2007). Constraints on mantle melting and composition and nature of slab components in volcanic arcs from volatiles (H_2O, S, Cl, F) and trace elements in melt inclusions from the Kamchatka Arc. *Earth and Planetary Science Letters* **255**, 53–69.

Righter, K. & Carmichael, I. S. E. (1993). Mega-xenocrysts in alkali olivine basalts: fragments of disrupted mantle assemblages. *American Mineralogist* **78**, 1230–1245.

Roberge, J., Delgado-Granados, H. & Wallace, P. J. (2009). Mafic magma recharge supplies high CO_2 and SO_2 gas fluxes from Popocatépetl volcano, Mexico. *Geology* **37**, 107–110.

Roggensack, K. (2001). Unraveling the 1974 eruption of Fuego volcano (Guatemala) with small crystals and their young melt inclusions. *Geology* **29**, 911–914.

Roggensack, K., Hervig, R. L., McKnight, S. B. & Williams, S. N. (1997). Explosive basaltic volcanism from Cerro Negro volcano: Influence of volatiles on eruptive style. *Science* **277**, 1639–1642.

Rondenay, S., Abers, G. A. & van Keken, P. E. (2008). Seismic imaging of subduction zone metamorphism. *Geology* **36**, 275–278.

Rüpke, L. H., Morgan, J. P., Hort, M. & Connolly, J. A. D. (2002). Are the regional variations in Central American arc lavas due to differing basaltic versus peridotitic slab sources of fluids? *Geology* **30**, 1035–1038.

Rüpke, L. H., Morgan, J. P., Hort, M. & Connolly, J. A. D. (2004). Serpentine and the subduction zone water cycle. *Earth and Planetary Science Letters* **223**, 17–34.

Sadofsky, S. J., Portnyagin, M., Hoernle, K. & van den Bogaard, P. (2008). Subduction cycling of volatiles and trace elements through the Central American volcanic arc: evidence from melt inclusions. *Contributions to Mineralogy and Petrology* **155**, 433–456.

Salters, V. J. M. & Stracke, A. (2004). Composition of the depleted mantle. *Geochemistry, Geophysics, Geosystems* **5**, Q05B07, doi:10.1029/2003GC000597.

Scambelluri, M., Muntener, O., Ottolini, L., Pettke, T. T. & Vannucci, R. (2004). The fate of B, Cl and Li in the subducted oceanic mantle and in the antigorite breakdown fluids. *Earth and Planetary Science Letters* **222**, 217–234.

Schaaf, P., Stimac, J., Siebe, C. & Macias, J. L. (2005). Geochemical evidence for mantle origin and crustal processes in volcanic rocks from Popocatepetl and surrounding monogenetic volcanoes, central Mexico. *Journal of Petrology* **46**, 1243–1282.

Schmidt, M. W. & Poli, S. (2004). Generation of mobile components during subduction of oceanic crust. In: Rudnick, R. L., Hollard, H. D. & Turekian, K. K. (eds) *Treatise on Geochemistry Volume 3: The Crust*. Amsterdam: Elsevier, pp. 567–591.

Schurr, B., Asch, G., Rietbrock, A., Trumbull, R. & Haberland, C. (2003). Complex patterns of fluid and melt transport in the central Andean subduction zone revealed by attenuation tomography. *Earth and Planetary Science Letters* **215**, 105–119.

Siebe, C., Rodriguez-Lara, V., Schaaf, P. & Abrams, M. (2004). Geochemistry, Sr–Nd isotope composition, and tectonic setting of Holocene Pelado, Guespalapa and Chichináutzin scoria cones, south of Mexico City. *Journal of Volcanology and Geothermal Research* **130**, 197–226.

Singer, B. S., Jicha, B. R., Leeman, W. P., Rogers, N. W., Thirwall, M. F., Ryan, J. & Nicolaysen, K. E. (2007). Along-strike trace element and isotopic variation in Aleutian Island arc basalt: Subduction melts sediments and dehydrates serpentine. *Journal of Geophysical Research* **112**, B06206, doi:10.1029/2006JB004897.

Sisson, T. W. & Bronto, S. (1998). Evidence for pressure-release melting beneath magmatic arcs from basalt at Galunggung, Indonesia. *Nature* **391**, 883–886.

Sisson, T. W. & Grove, T. L. (1993). Experimental investigations of the role of H_2O in calc-alkaline differentiation and subduction zone magmatism. *Contributions to Mineralogy and Petrology* **113**, 143–166.

Sisson, T. W. & Layne, G. D. (1993). H_2O in basalt and basaltic andesite glass inclusions from four subduction-related volcanoes. *Earth and Planetary Science Letters* **117**, 619–635.

Sobelev, A. V. & Chaussidon, M. (1996). H_2O concentrations in primary melts from supra-subduction zones and mid-ocean ridges; implications for H_2O storage and recycling in the mantle. *Earth and Planetary Science Letters* **137**, 45–55.

Spandler, C., Hermann, J., Faure, K., Mavrogenes, J. A. & Arculus, R. J. (2008). The importance of talc and chlorite 'hybrid' rocks for volatile recycling through subduction zones; evidence from the high-pressure subduction mélange of new Caledonia.

Contributions to Mineralogy and Petrology **155**, doi:10.1007/s00410-007-0236-2.

Spilliaert, N., Métrich, N. & Allard, P. (2006). S–Cl–F degassing pattern of water-rich alkali basalt: Modelling and relationship with eruption styles on Mount Etna volcano. *Earth and Planetary Science Letters* **248**, 772–786.

Staudigel, H., Davies, G. R., Hart, S. R., Marchant, K. M. & Smith, B. M. (1995). Large-scale isotopic Sr, Nd and O isotopic anatomy of altered oceanic crust—DSDP/ODP sites 417/418. *Earth and Planetary Science Letters* **130**, 169–185.

Stolper, E. & Newman, S. (1994). The role of water in the petrogenesis of Mariana trough magmas. *Earth and Planetary Science Letters* **121**, 293–325.

Straub, S. M., LaGatta, A. B., Pozzo, A. L. M.-D. & Langmuir, C. H. (2008). Evidence from high-Ni olivines for a hybridized peridotite/pyroxenite source for orogenic andesites from the central Mexican Volcanic Belt. *Geochemistry, Geophysics, Geosystems* **9**, doi:10.1029/2007GC001583.

Sun, S. & McDonough, W. F. (1989). Chemical and isotopic systematics of oceanic basalts: implications for mantle composition and processes. In: Saunders, A. D. & Norry, M. J. (eds) *Magmatism in the Ocean Basins. Geological Society, London, Special Publications* **42**, 313–345.

Suter, M., Martinez, M. L., Legorreta, O. Q. & Martinez, M. C. (2001). Quaternary intra-arc extension in the central Trans-Mexican volcanic belt. *Geological Society of America Bulletin* **133**, 693–703.

Tatsumi, Y. & Eggins, S. (1995) *Subduction Zone Magmatism*. Oxford: Blackwell, 211p.

Tenthorey, E. & Hermann, J. (2004). Composition of fluids during serpentinite breakdown in subduction zones; evidence for limited boron mobility. *Geology* **32**, 865–868.

Toplis, M. J. (2005). The thermodynamics of iron and magnesium partitioning between olivine and liquid: criteria for assessing and predicting equilibrium in natural and experimental systems. *Contributions to Mineralogy and Petrology* **149**, 22–39.

Uribe-Cifuentes, R. M. & Urrutia-Fucugauchi, J. (1999). Paleomagnetic study of the Valle de Santiago volcanics, Michoacán–Guanajuato volcanic field, Mexico. *Geofisica Internacional* **38**, 217–230.

Valley, J. W., Kitchen, N., Kohn, M. J., Niendorf, C. R. & Spicuzza, M. J. (1995). UWG-2, a garnet standard for oxygen isotope ratio: Strategies for high precision and accuracy with laser heating. *Geochimica et Cosmochimica Acta* **59**, 5223–5231.

Vigouroux, N., Wallace, P. J. & Kent, A. J. R. (2008). Volatiles in high-K magmas from the Western trans-Mexican volcanic belt: Evidence for fluid fluxing and extreme enrichment of the mantle wedge by subduction processes. *Journal of Petrology* **49**, 1589–1618.

Wade, J. A., Plank, T., Melson, W. G., Soto, G. J. & Hauri, E. H. (2006). The volatile content of magmas from Arenal volcano, Costa Rica. *Journal of Volcanology and Geothermal Research* **157**, 94–120, doi:10.1016/j.jvolgeores.2006.03.045.

Walker, J. A., Roggensack, K., Patino, L. C., Cameron, B. I. & Matais, O. (2003). The water and trace element contents of melt inclusions across an active subduction zone. *Contributions to Mineralogy and Petrology* **146**, 62–77.

Wallace, P. J. (1998). Water and partial melting in mantle plumes: inferences from the dissolved H_2O concentrations of Hawaiian basaltic magmas. *Geophysical Research Letters* **25**, 3639–3642.

Wallace, P. J. (2005). Volatiles in subduction zone magmas; concentrations and fluxes based on melt inclusion and volcanic gas data. *Journal of Volcanology and Geothermal Research* **140**, 217–240.

Wallace, P. J. & Carmichael, I. S. E. (1994). Sulfur speciation submarine basaltic glasses as determined by measurements of SKα X-ray wavelength shifts. *American Mineralogist* **79**, 161–167.

Wallace, P. J. & Carmichael, I. S. E. (1999). Quaternary volcanism near the Valley of Mexico; implications for subduction zone magmatism and the effects of crustal thickness variations on primitive magma compositions. *Contributions to Mineralogy and Petrology* **135**, 291–314.

Workman, R. K. & Hart, S. R. (2005). Major and trace element composition of the depleted MORB mantle (DMM). *Earth and Planetary Science Letters* **231**, 53–72.

Wysoczanski, R. J., Wright, I. C., Gamble, J. A., Hauri, E. H., Luhr, J. F., Eggins, S. M. & Handler, M. R. (2006). Volatile contents of Kermadec Arc–Havre Trough pillow glasses: Fingerprinting slab-derived aqueous fluids in the mantle sources of arc and back-arc lavas. *Journal of Volcanology and Geothermal Research* **152**, 51–73, doi:10.1016/j.jvolgeores.2005.04.021.

Yang, T., Grand, S. P., Wilson, D., Guzman-Speziale, M., Gomez-Gonzalez, J. M., Dominguez-Reyes, T. & Ni, J. (2009). Seismic structure beneath the Rivera subduction zone from finite-frequency seismic tomography. *Journal of Geophysical Research* **114**, B01302, doi:10.1029/2008JB005830.